5-8-2014

Life-Oriented Controller Design in Ocean Tidal Power Applications

Zhibing Zhao
zhaozb08@gmail.com

Life-Oriented Controller Design in Ocean Tidal Power Applications

Zhibing Zhao

B.A., Electrical Engineering, Tsinghua University, Beijing, China, 2012

A Thesis
Submitted in Partial Fulfillment of the
Requirements for the Degree of
Master of Science
At the
University of Connecticut

2014

APPROVAL PAGE

Master of Science Thesis

Life-Oriented Controller Design in Ocean Tidal Power Applications

Presented by

Zhibing Zhao, B.A. Electrical Engineering

Major Advisor _____

Peng Zhang

Associate Advisor _____

Shengli Zhou

Associate Advisor _____

Jun-Hong Cui

University of Connecticut

2014

Dedication

This thesis is dedicated to my parents, who encouraged me a lot when I felt frustrated, when I had difficulties, and when I was homesick. It is also dedicated to my girlfriend Nian for her accompany and good suggestions.

Acknowledgements

I would like to thank my major advisor, Prof. Peng Zhang for his insightful advice on my research, my work, and my life. I have spent two fruitful years at Prof. Zhang's lab, and have learned to use the hardware and software in my research, to communicate with people, and to manage my time. When writing my thesis, Prof. Zhang provided a lot of good comments and kind encouragement.

I would also like to thank Prof. Shengli Zhou and Prof. Jun-Hong Cui, who help a lot in my paper, my presentation, and my thesis writing. Prof. Zhou told me that, achievements come from hard work.

Last but not least, I would thank Prof. Xiaoyu Wang for his help in small signal analysis, Xiaoka Xu, Jian Zhang, Taofeek Orekan and Lingyu Ren for their contributions in sensors and simulations.

Contents

List of Tables

List of Figures

Abstract

Ocean energy is developing fast in recent years. Tidal currents have the advantage of predictability over the others, and gain attentions all over the world.Tidal currents can turn a turbine, and therefore drive a generator for electricity. One problem in tidal current power conversion is the lifespan of the system. Due to the high density of sea water, large mechanical torques are applied on the turbine blades and the shaft. These torques cause damages in the system, and may lead to failures.

In this thesis, a hybrid control strategy is proposed to extend the lifespan of the tidal system. This strategy is a mixture of maximum power point and constant torque control. Small signal analysis is performed to provide directions for control parameters design. Performance of the proposed strategy is compared with pure maximum power point strategy through simulations. The lifespan of the system under the proposed strategy can be tens of times longer.

Chapter 1

Introduction

The ocean has been providing resources for human for centuries. It supplies delicious fish, minerals such as salt and sand, and fossil fuels such as crude oil; It produces oxygen and deposit carbon dioxide; It regulates the climate, and is an essential part in water circulation. Sensors play an important role in observing and exploiting the ocean. Application of sensors include oil industry, climate observation, study of marine environment and life [1]. These sensors form an underwater sensor network. Most sensors need power supply for communication purpose. Currently these sensors are supplied with batteries, which need maintenance and replacement regularly, therefore power consumption is an important metric for sensor node design [2]. Ocean energy harnessment is developing very fast in recent years. But there are still difficulties for commercial use due to its cost, stability, and reliability reasons. This thesis aims to enhance the reliability of ocean energy instruments.

This chapter introduces the background and motivations of this research. Offshore and underwater electric loads will be introduced next, followed by a review of ocean energy. The next section focuses on tidal current energy, which is the main topic of this thesis.

1.1 Offshore and Underwater Power Demand

Continents are equipped with power systems, which provide electricity to most onshore loads. However, there is almost no power grid over or under the ocean to supply the offshore load, such as oil platforms and underwater sensor networks. This section introduces the current status of this two types of electric loads.

1.1.1 Offshore Oil Platforms

Installation of an offshore oil platform demands electric power of megawatts level. It cannot be supplied by AC transmission system due to the long distance, either by high voltage DC transmissions system because of its control complexity [3]. Thus local power generation is preferred. Gas turbines or diesels are able to supply that amount of power, but they produce carbon dioxide and their efficiency is low. Ocean energy may be a solution, and will be introduced in the next section.

1.1.2 Underwater Sensor Networks

This section briefly summarizes the current status of underwater sensor networks, to show the importance of sensor networks to human, and the necessity to supply power to these sensors. In the past several years, the physical layer of underwater acoustic sensor networks has been making a great progress and turning to mature, as orthogonal frequency-division multiplexing (OFDM) [4] [5] [6] [7] [8] [9], single carrier modulation [10], and spread spectrum [11] techniques have been extensively investigated. At the same time, the focuses of research interest have been shifting the network protocol and the application of underwater acoustic sensor networks, such as localization scheme [12]. Detailed review of sensor networks can be found in [13] [14].

Underwater sensors assist exploring and monitoring the ocean in many aspects. In terms of water quality, they measure temperature, water density, salinity, acidity, conductivity, turbidity, oxygen, hydrogen, dissolved methane gas, and also pollution. Underwater sensor network is able to collect data in four dimensions (spacial and time). In terms of resource detection, sensors can discover oilfields, explore minerals, and determine routes for undersea cables. They also monitor seismic activity and report submarine earthquakes. Moreover, they have applications in navigation and protection from attacks.

These applications require sensors to have the ability to process signals, exchange information, and relay data to an onshore station. Mobile sensors need to be powered to move in the water. A typical sensor structure is shown in Fig. 1 [14]. Green arrows represent communications between blocks and red arrows show power flow. Most blocks consume electric power.

Batteries are able to provide stable power to these sensors, and is currently widely used. But they need regular maintenance and replacement, which is difficult for underwater equipment. Ocean energy is quite available but relatively difficult to harness. Different forms of energy converters are developing very fast recently. The next section is to review the current status of them.

1.2 Ocean Energy

The ocean covers 70% of the earth and has abundant resources, which are not efficiently made use of. Ocean energy is especially hard to utilize because of the harsh environment underwater. Due to the energy crisis and the huge potential of the ocean, people got interested in ocean energy in spite of these difficulties. Research is being carried out

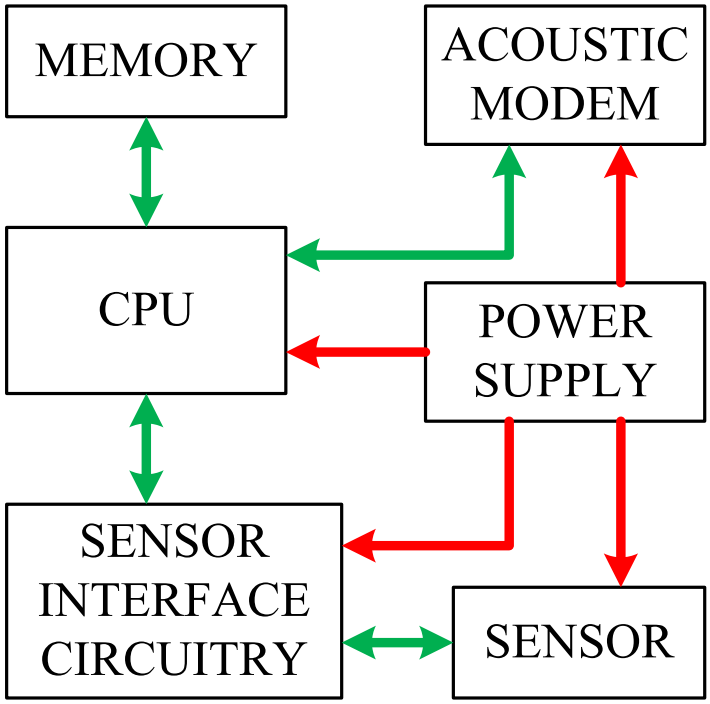

Figure 1: Typical sensor structure

and prototypes are under development [15]. Test sites were built all over the world in Europe, US, Australia, and China [16]. In this section, four main types of ocean energy converters are introduced and reviewed.

1.2.1 Tidal Current Power

Tides are created by the interaction among the gravitational forces of the sun, the Earth, and the moon. The moon has 2.17 times the effect of the sun due to the mass and distance differences, thus determining the direction of the tides, while the sun affects the magnitude of tides. The force of the moon (or the sun) has the strongest effect on water molecules closest to the moon, and the weakest effect on one at the opposite side of the earth, resulting in high tides in both directions. The rotation of the earth causes tidal currents in rivers and oceans [17] [18]. Generally the periods of tides are half a

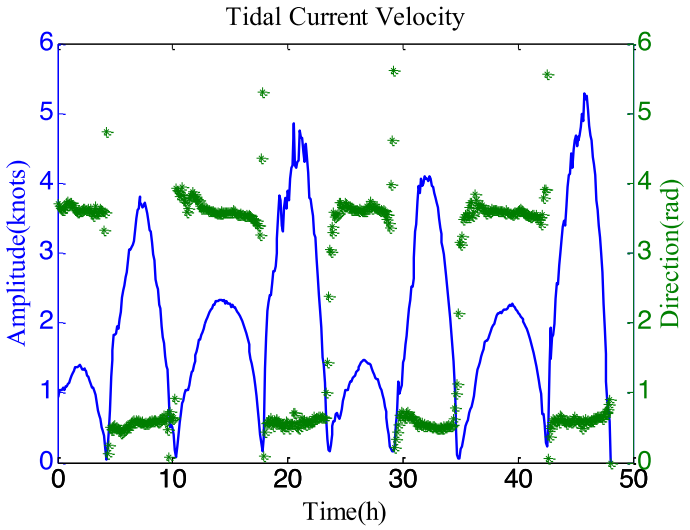

Figure 2: Tidal current data at Lituya Bay entrance

day (semidiurnal), one day (diurnal) or a mixture of the two [19]. In addition, there are other periodic components such as 14 days, half a year or even longer depending on the locations [18]. Tidal currents are both predictable and consistent. It is estimated that 3TW of tidal power is available but less than 3% is suitable for power generation [20].

Tidal current speed changes from season to season, and varies from site to site. Site evaluation and selection is necessary for tidal generators [21]. Fig. 2 depicts the tidal current velocity data measured at the Lituya Bay entrance from July 4th, 2008 through July 5th, 2008, at the depth of 4.88m. The blue line is the magnitude of tidal current speed and the green dots are the directions of tidal flow. Tidal currents flow mainly in two opposite directions.

The horizontal axis turbine is the main energy converter to harness tidal current power. Tidal currents drive a turbine to rotate, and the turbine drives an electric generator to generate variable AC electricity, which is transformed to the fundamental frequency through power electronic converters.

Tidal current power converter is already commercialized. Different from wave energy,

tidal turbines are used in most companies. Several major companies will be introduced next to demonstrate the current status. A good summary can be found in [22].

The SeaGen S system was developed by Marine Current Turbines [23]. This 1.2MW system was installed in Strangford Lough in 2008, delivering 20MWh power per day. One feature of the system is that the turbines can be raised above water for maintenance. Andritz Hydro Hammerfest installed a 300kW turbine at Kvalsundet in Finnmark, Norway, which has 17000 hours' operation record. A 1MW pre-commercial turbine is under development. IT Power installed the first commercial scale marine current turbine in 2003 [24]. Verdant Power designed a 5m diameter horizontal axis tidal current turbine [25]. Open Hydro developed the open-centre turbine for tidal current power. This type of turbine is simple and lubricant-free, which is suitable for underwater environment [26]. Clean Current made the 0.8MW in-stream tidal current turbine [27].

1.2.2 Other Forms of Ocean Energy

Wave Power

Waves are caused by wind, atmospheric pressure, earthquakes etc., among which the ones caused by wind are the most common. The interactions between the water surface air molecules and the water molecules creates ripples, which gradually grow to waves. Waves travel long distances and thus are predictable.

The potential wave power in the world is 1-10TW, and only 2TW is availalbe [28] [20]. Compared with wind, wave power is more predictable and highly available up to 90% of the time [29]. Wave energy converter can be classified into three categories according to their locations: shoreline, nearshore and offshore. The longer the distance from the shore, the higher the power is available, but the higher the cost will be. Recent developments

of wave energy converters include modeling [30] and control assessment [31].

Thermal Power

The potential of thermal energy was estimated to be 10TW [29] or 7TW [32] as a later estimate under the condition that it will not affect the ocean ecosystem. Ocean thermal energy conversion (OTEC) not only generates electricity, but also provides fresh water, cold water for industrical cooling and air conditioning. On the other hand, OTEC requires that the temperature difference between surface seawater and 1000m deep is about 20°C [33]. There are two basic types of conversion methods, closed-cycle and open-cycle. The working principles are similar, to use the heat in the warm surface water to create steam, which is able to drive a turbine. Then cold water condense the steam back to liquid.

In a open-cycle OTEC, the sea water itself is the working fluid. Warm sea water is pumped into a low air pressure environment where it will boil immediately. The steam then drives a turbine and generator system to generate electricity. After that the steam is cooled down and condensed to water. The water obtained here is desalinated.

Osmotic Power

The power of osmosis is from salinity gradient between two sides of a semi-permeable membrane. Water will flow to the saltier side through the membrane. This will increase the volume on the saltier side, which can be used to generate power. The osmotic power potential is 1655 TWh/year [34]. The pressure retarded osmosis (PRO) is very promising for osmotic power generation.

1.3 Motivation of this Research

Among ocean energy conversions, wave power and tidal current power are more attractive to the industry. And tidal current power has the advantage of predictability. The Bay of Fundy on the Atlantic coast of North America has the highest tides in the world, and many companies have built or are building tidal turbines there. In 2009, a $ 10-million turbine from Nova Scotia Power was destroyed by tidal flows in less than one month.

It is very expensive to build and maintain an underwater power generation system due to the harsh underwater environment [35]. The density of water is about 800 times of that of air, and the rotating speed of a tidal turbine is generally 0.32 times that of a wind turbine under the same power ratings [36]. These features make the mechanical torque of a tidal turbine 3 times that of a wind turbine. It is easy for an underwater system to fail but it is difficult to repair. Reliability becomes a critical consideration during design and operation.

Reliability of the blades and shaft in a turbine-generator system has drawn attention for decades. Reliability models of tidal systems were built in [37]. Shaft fatigue and life expenditure under system fault were analyzed in [38] [39] [40]. As renewable generation has developed fast recently, the impact of variable frequency torques is studied in [41]. In a tidal turbine-generator system, the rotating speed varies as the tidal current speed changes, resulting in cyclic stress on the shaft and turbine blades. In other ocean energy converters, turbines are also widely used. The strategy proposed in this thesis may also be applied.

In this thesis, a hybrid control strategy is proposed based on a tidal turbine generation system. Reliability of the shaft system is especially considered. In [42], the authors introduced three control strategies in wind power generation: constant power control, constant torque control and maximum power point tracking. Constant power control

cannot capture as much energy as the other two, which is not desirable. The maximum power point tracking control is able to draw more power than other strategies, but it applies greater torque on the turbine blades and shaft. The strategy proposed in this paper is a hybrid one, combining the maximum power point strategy and the constant torque strategy. It is compared with the pure maximum power point tracking strategy by real-time simulations. Under this strategy, the life cycle of the tidal power generation system is extended and maintenance costs are reduced. In the long run, more power is generated.

The rest of this thesis is organized as follows. In the second chapter, the models of both mechanical and electrical parts of the system are provided. The proposed control strategy is explained and compared in the third chapter. In the fourth chapter small signal analysis is performed. The fifth chapter explains simulation tools and results. The last chapter concludes that the proposed control strategy is able to extend the life cycle of the system.

1.4 Summary

This chapter first lists the main electricity demand in the ocean, both above and underwater. Then major ocean energy converters are introduced, including their working principles and developments in industry. Finally, the motivations of this researsh are stated. This thesis is to emphasize the control strategy to extend the lifespan of ocean energy converters.

The publication related to this thesis is [43]

Chapter 2

System Configuration and Modeling

The system configuration is shown in Fig. 3. The permanent magnet synchronous generator (PMSG), which is driven by the tidal current turbine, is connected to the grid through a back-to-back converter. This chapter provides models for all components in this system. Also, this chapter provides the basis for torque analysis and controller design in Chapter 3 and small signal analysis in Chapter 4.

2.1 Tidal Current Turbines

There are two major types of turbines used in tidal current energy converters according to the direction of the turbine axis. A review on tidal current turbines can be found in [44]. This thesis uses horizontal axis turbines due to their industry applications.

The turbine model is

$$P = 0.5\rho\pi R^2 v^3 C_p(\lambda), \tag{2.1}$$

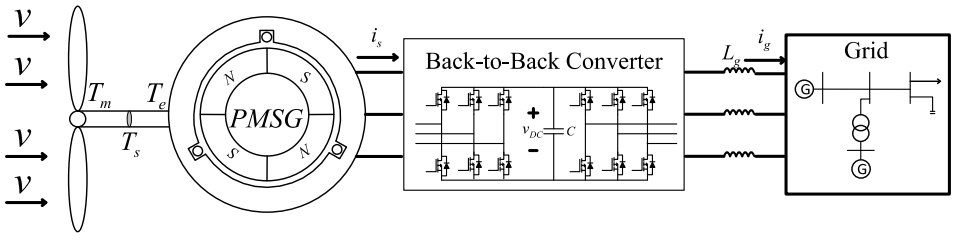

Figure 3: Tidal system configuration

Table 1: Power Coefficient Parameters

Parameter	Value
c_5	-6.162483×10^{-4}
c_4	0.012
c_3	-0.0861
c_2	0.2383
c_1	-0.0884
c_0	0.0112

where P is the captured power by the turbine. R is the radius of the turbine rotor. v is the speed of tidal currents. $C_P(\lambda)$ is called power coefficient, which describes the efficiency of the turbine to absorb power from tidal currents. λ is tip speed ratio, which is defined as

$$\lambda = \frac{\omega R}{v}, \tag{2.2}$$

where ω is the rotating speed of the turbine.

The expression of power coefficient is

$$C_p(\lambda) = c_5\lambda^5 + c_4\lambda^4 + c_3\lambda^3 + c_2\lambda^2 + c_1\lambda + c_0, \tag{2.3}$$

where c_0 to c_5 are constants. The power coefficient curve is from [45] and a polynomial (2.3) is used to fit this curve. The values used in this thesis are listed in Table 1. A typical power coefficient curve is shown in Fig. 4. The power coefficient has a maximum within the Betz's limit at a specific tip speed ratio.

The mechanical torque T_m from the tidal currents is

$$T_m = \frac{P}{\omega} \tag{2.4}$$

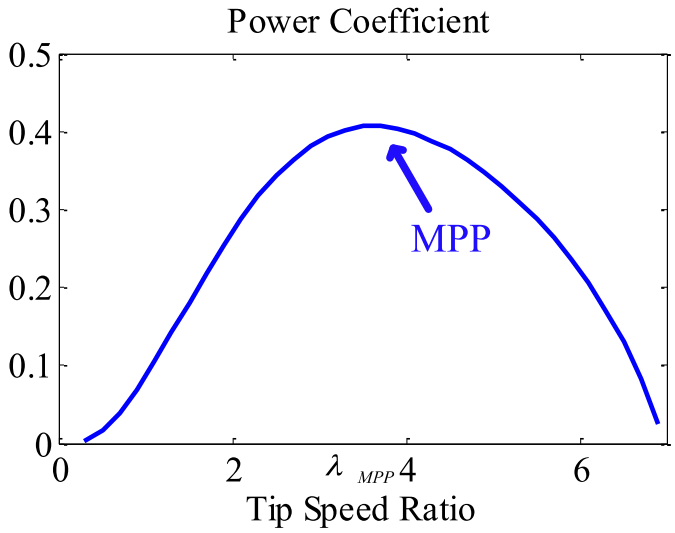

Figure 4: Typical power coefficient curve

2.2 Permanent Magnet Synchronous Generator

Permanent magnet synchronous generators (PMSG) and doubly-fed induction generators (DFIG) both have wide applications in renewable generations. A comparison of PMSG and DFIG is provided in [46], showing that the PMSG has advantages in tidal current converters. Studies on PMSG have been carried out in [47] [48] [49]. Models of PMSG can be found in literatures, including models under ABC reference frame [50] and dq reference frame. This thesis uses the permanent magnet synchronous machine model in Simulink.

Table 2: PMSG Parameters

Parameter	Value	Unit
p	24	
R_s	3.53	Ω
L_d	0.0782	H
L_q	0.0782	H
ϕ_m	0.91781	Wb

The model of the permanent magnet synchronous generator is

$$v_{ds} = R_s i_{ds} + L_d \frac{di_{ds}}{dt} - p\omega L_q i_{qs} \tag{2.5}$$

$$v_{qs} = R_s i_{qs} + L_q \frac{di_{qs}}{dt} + p\omega L_d i_{ds} \tag{2.6}$$

$$P_e = -1.5(v_{ds} i_{ds} + v_{qs} i_{qs}) \tag{2.7}$$

$$T_e = -\frac{3}{2} p\psi_m i_{qs}, \tag{2.8}$$

where R_s is the stator resistance. L_d and L_q are the stator d-axis inductance and q-axis inductance. p is the number of pole pairs. ψ_m is the magnetic flux of the permanent magnet. v_{ds}, v_{qs} are the stator d-axis and q-axis voltages and i_{ds}, i_{qs} are the stator d-axis and q-axis currents. ω is the rotating speed of the generator, which is the same as that of the turbine. P_e is the electric power and T_e is the electromagnetic torque. Parameters used in the simulations are shown in Table 2

2.3 Drive Train

The drive train is the most critical part in this system. This chapter only provides the model of the drive train system. Detailed analysis will be provided in the next chapter. In the turbine-generator system, mechanical torque is applied on turbine blades, and electromagnetic torque on the generator in the opposite direction. To simplify the

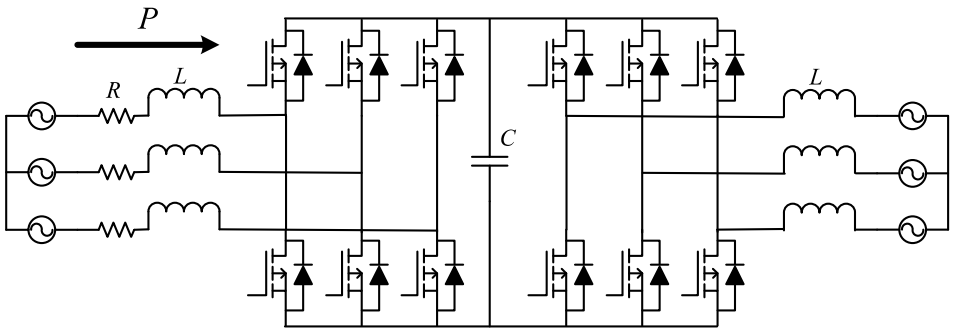

Figure 5: Back-to-back converter

problem, it is assumed that the whole drive train rotates at the same speed. Friction omitted, we get

$$J\frac{d\omega}{dt} = T_m - T_e, \tag{2.9}$$

where J is the combined moment of inertia of the drive train system, which consists of the turbine and the rotor of the PMSG.

2.4 Back-to-Back Converter

This section only provide the average model of the back-to-back converter for small signal analysis purpose. Simulink inverter blocks are used in simulations. A detailed modeling procedure can be found in [51]. A typical back-to-back converter is shown in Fig. 5. The two converters on the left and right of the capacitor are the rectifier and the inverter, respectively. In this thesis, they are also referred to as machine side converter (MSC) and grid side converter (GSC). In the tidal current energy conversion system, the rectifier is connected to the generator directly, while the inverter is connected to the grid through a filter, as is seen in Fig. 3.

For the machine side converter, the average model is

$$v_{ds} = d_{ds} v_{DC} \tag{2.10}$$

$$v_{qs} = d_{qs} v_{DC}, \tag{2.11}$$

where d_{ds} and d_{qs} are the d-axis and q-axis duty cycles. v_{DC} is the DC link voltage. The average model of the grid side converter is

$$u_{dg} = v_{dg} + L_g \frac{di_{dg}}{dt} - \omega_g L_g i_{qg} \tag{2.12}$$

$$u_{qg} = v_{qg} + L_g \frac{di_{qg}}{dt} + \omega_g L_g i_{dg}. \tag{2.13}$$

In the equations above, L_g is the inductance of the filter. v_{dg} and v_{qg} are the grid d-axis and q-axis voltages. i_{dg} and i_{qg} are the d-axis and q-axis currents to the grid. ω_g is the angular frequency of the grid voltage. u_{dg} and u_{qg} are the output d-axis and q-axis voltages of the grid side converters, which satisfies

$$u_{dg} = d_{dg} v_{DC} \tag{2.14}$$

$$u_{qg} = d_{qg} v_{DC}, \tag{2.15}$$

where d_{dg} and d_{qg} are the d-axis and q-axis duty cycles of the grid side converter. The model of DC link is

$$C v_{DC} \frac{dv_{DC}}{dt} = -\frac{3}{2} v_{ds} i_{ds} + v_{qs} i_{qs} - \frac{3}{2} v_{dg} i_{dg} \tag{2.16}$$

Table 3: Back-to-Back Converter Parameters

Parameter	Value	Unit
J	6.61	$\text{kg} \cdot \text{m}^2$
ω_g	120π	rad/s
L_g	1	mH
c	1	mF
v_{dg}	208	V
v_{qg}	0	V

.

The parameters in this section are provided in Table 3

2.5 Summary

This chapter briefly lists the model of all components in the system. It is the basis of the following chapters, including torque analysis controller design, and small signal analysis. The simulation model is very close to the mathematic descriptions in this chapter, though not exactly the same.

Chapter 3

Torque Analysis and Control Strategy

To predict the lifespan of the system, the mechanical torque and electromagnetic torque applied to the drive train is studied in this chapter. Based on the torque analysis, a hybrid control strategy is proposed.

3.1 Torque Analysis

This section analyzes stress and fatigue in the drive train. The mechanical torque and the electromagnetic torque determine the rotating speed of the drive train system, as is seen from Eqn. (2.9). The interaction of mechanical torque and electromagnetic torque causes stress on the turbine blades and the shaft, leading to fatigue or even failure. The relation between stress and the life cycle is described with an S-N curve. Above the fatigue limit, the number of cycles decreases exponentially with stress. Thus it is very beneficial to reduce stress on the shaft. Below the fatigue limit, lifespan of the shaft is considered as infinity. The transformation from stress to torque is provided in [39], which also provided Eqn. (3.1). A typical torque-life curve is shown in Fig. 6.

$$N = \frac{1}{2}\left(6.4 \times 10^{-6}\frac{\tau}{R_0^3}\right)^{-17.86} \tag{3.1}$$

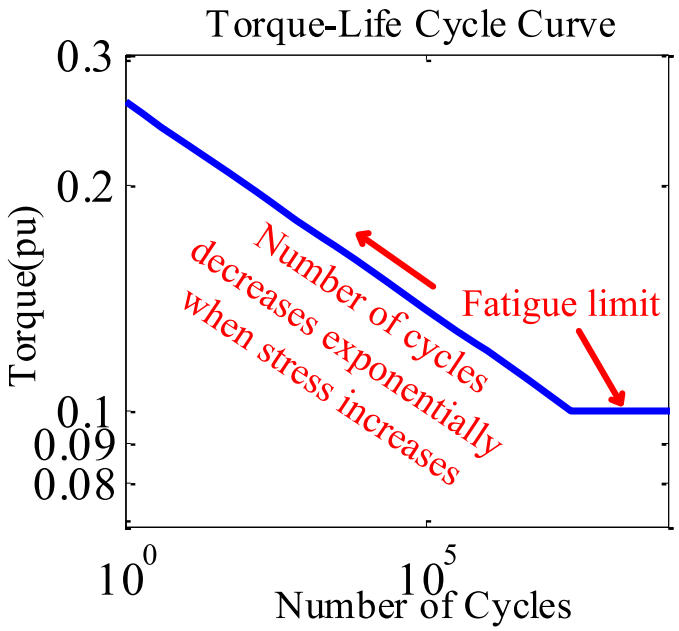

Figure 6: Typical torque-life curve

N is the number of cycles the shaft can endure. R_0 is the radius of the shaft. τ is the maximum torque in each cycle. Formula (3.1) is used to estimate the life cycle of the shaft under the assumption that the material is the same as in [39].

To analyze the torque on the shaft, we consider the torque at a cross section s in the shaft, which is T_s. The drive train system is shown in Fig. 7

The mechanical equations are

$$J_1 \frac{d\omega}{dt} = T_m - T_s \tag{3.2}$$

$$J_2 \frac{d\omega}{dt} = T_s - T_e \tag{3.3}$$

where J_1 and J_2 are the moments of inertia left of the section and right of the section, respectively.

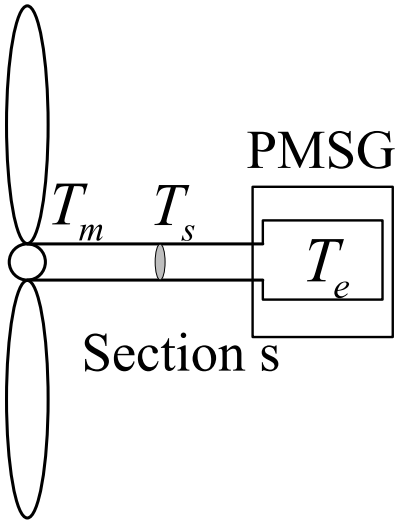

Figure 7: Drive train system

Substitute (3.2) into (3.3), and we get

$$T_s = \frac{J_1 T_e + J_2 T_m}{J_1 + J_2} \tag{3.4}$$

In (3.4), J_1 is mainly the moment of inertia of the tidal turbine J_T, and J_2 is mainly that of the generator J_G. And consider

$$J_1 + J_2 = J, \tag{3.5}$$

thus we get,

$$T_s = \frac{J_T T_e + J_G T_m}{J} \tag{3.6}$$

As is seen in literature, J_T can reach a value as high as 10^4 kg $\cdot$ m^2 [52], whereas J_G is generally 10^{-3}kg m^2, which is not comparable to even a small scale tidal turbine. Thus T_s is mainly determined by T_e.

Stress on turbine blades is determined by mechanical torque, electromagnetic torque

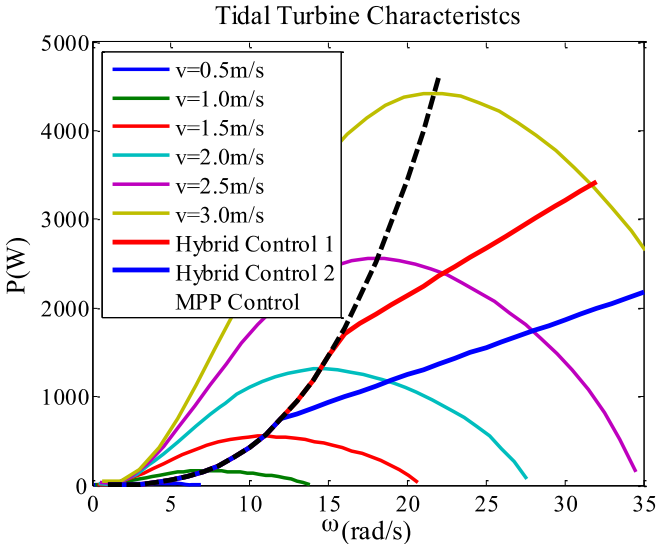

Figure 8: Tidal turbine characteristics

and turbine structure, which is rather more complex than that on the shaft. In this thesis, we simply consider the effect of mechanical torque.

3.2 Control Strategy

In tidal current power generation systems, the maximum power point tracking strategy is popular and studied in [53]. The concept of life extending control was proposed in [54], and applied in wave generators in [55] [56]. In tidal current energy applications, power limitation control and power smoothing control were proposed in [57] [58] [59]. This thesis applies the life extending control strategy to the tidal current energy converter.

3.2.1 Control Strategy

The control strategy is designed based on tidal turbine characteristics. Fig. 8 depicts tidal turbine characteristics at different tidal speeds. Under the maximum power point (MPP) strategy, the operating point of the system is on the black dashed line. The

mechanical torque is the slope of the straight line connecting the operating point to the origin. It rises fast as the operating point goes up along the maximum power point line. When tidal speed is very high, eg. 3m/s, the mechanical torque is very large. At the steady state, the electromagnetic torque fluctuates around the mechanical torque, and adds to the stress on the shaft and turbine blades.

To mitigate the stress, a hybrid control strategy, which combines the maximum power point strategy and the constant torque strategy, is proposed. The operating trace is shown as the red line or the blue line in Fig. 8. At low tidal current speeds, the hybrid strategy tracks the maximum power point. Then at a certain point, it turns and starts to track a straight line, whose extension in the opposite direction passes the origin.

Compared to hybrid control 1, the hybrid control 2 applies lower torques on the shaft and the blades, but captures less power. Designers should select one strategy that fits the strength of the shaft.

3.2.2 Realization of Control Strategy

Realization of this strategy is straightforward. Power and rotating speed are used to estimate tidal current speed, and then the reference rotating speed is generated from the tidal current speed, where Neural network blocks are used. PI controllers regulate the rotating speed of the generator.

Tidal Current Speed Estimation and Reference Generation

Tidal current speed is necessary for the controller to generate the reference rotating speed of the turbine. But the tidal current sensor is expensive to install and maintain underwater. Thus we tried to estimate the tidal current speed with the captured power and rotating speed. As Fig. 8 shows, each $P - \omega$ pair corresponds to a tidal current

speed. Due to the nonlinearity of the power coefficient, it is difficult to get the explicit function $v = f(P, \omega)$. So a feed forward neural network is used to realize this function.

The neural network is composed of several layers. A hidden layer consists of neurons. A neuron with a vector input is shown in Fig. 9. p_1, p_2, ..., p_R are elements of the input vector $\mathbf{P}$.

$$\mathbf{P} = \begin{bmatrix} p_1 \\ p_2 \\ \vdots \\ p_R \end{bmatrix}. \tag{3.7}$$

The weight vector is

$$\mathbf{W} = \begin{bmatrix} w_1 & w_2 & \cdots & w_n \end{bmatrix}. \tag{3.8}$$

The output a is

$$a = f(\mathbf{W}\mathbf{p} + b), \tag{3.9}$$

where b is a scalar bias. Both the weight and the bias are adjustable so that the neural network can be trained. f is called tranfer function. Different transfer functions are used in different layers, for different purposes. Detailed introduction can be found in [60].

If multiple neurons are included in a hidden layer, the structure is shown in Fig. 10. The output of this layer is

$$\mathbf{a} = \mathbf{f}(\mathbf{W}\mathbf{p} + \mathbf{b}), \tag{3.10}$$

where

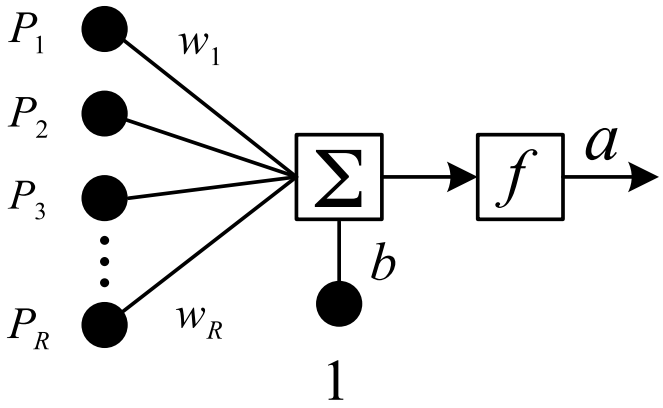

Figure 9: One neuron with a vector input

$$\mathbf{a} = \begin{bmatrix} a_1 \\ a_2 \\ \vdots \\ a_R \end{bmatrix}, \tag{3.11}$$

$$\mathbf{b} = \begin{bmatrix} b_1 \\ b_2 \\ \vdots \\ b_R \end{bmatrix}, \tag{3.12}$$

$$\mathbf{W} = \begin{bmatrix} w_{11} & w_{12} & \cdots & w_{1R} \\ w_{21} & w_{22} & \cdots & w_{2R} \\ \vdots & \vdots & \ddots & \vdots \\ w_{R1} & w_{R2} & \cdots & w_{RR} \end{bmatrix}. \tag{3.13}$$

The output of this hidden layer will go to the next layer and finally produce a scalar output. There may be multiple hidden layers in a neural network, but it is out of the

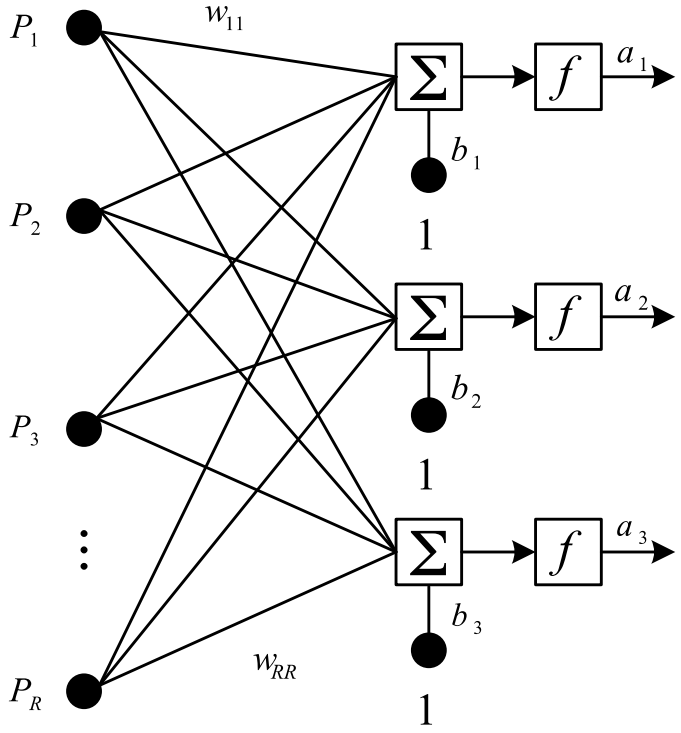

Figure 10: Multiple neurons in one hidden layer

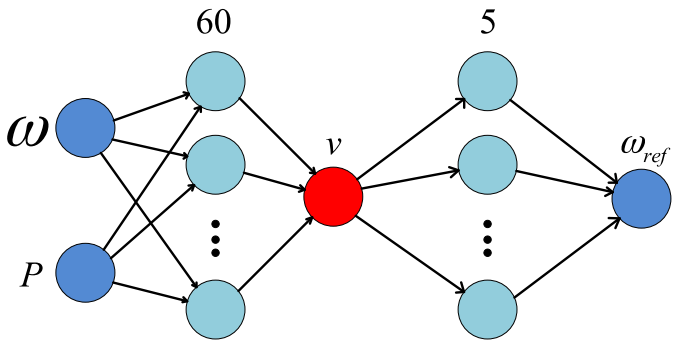

Figure 11: Neural network used in the controller

scope of this thesis. The parameters **W** and **b** are invisible to users in the MATLAB toolbox. They are adjusted when the neural network is being trained.

To train the neural network, the user must collect data first. For this tidal system, the data was generated from each characteristic curve in Fig. 8, and was used to train a feed forward neural network to estimate the tidal current speed. In this stage (speed estimation), one hidden layer of 60 neurons is used, as is shown in Fig. 11. In the next stage (reference generation), another neural network with one hidden layer of 5 neurons is used to generate the reference rotating speed.

Table 4 illustrates the data to train the neural networks for reference rotating speed generation. The first colomn is tidal current speed, which is the input of the neural network. The second and third columns are the outputs for maximum power point control and hybrid control, respectively. It is seen that when the tidal current speed is under 2.2m/s, the outputs of the two neural networks are the same. For high tidal current speed over 2.3m/s, the rotating speed under hybrid control is higher.

Part of the data for speed estimation stage at tidal current speed $v = 2.5$m/s are listed in Table. 5. The inputs are the second and the third columns, and the output for this piece of data is 2.5. The selection of λ determines how the data are generated.

Table 4: Data for Reference Generation Stage

Tidal Current Speed	MPP control	Hybrid Control
0.1	0.72	0.72
0.2	1.44	1.44
0.3	2.16	2.16
0.4	2.88	2.88
0.5	3.60	3.60
0.6	4.32	4.32
0.7	5.04	5.04
0.8	5.76	5.76
0.9	6.48	6.48
1.0	7.20	7.20
1.1	7.92	7.92
1.2	8, 64	8, 64
1.3	9.36	9.36
1.4	10.08	10.08
1.5	10.80	10.80
1.6	11.52	11.52
1.7	12.24	12.24
1.8	12.96	12.96
1.9	13.68	13.68
2.0	14.40	14.40
2.1	15.12	15.12
2.2	15.84	15.84
2.3	16.56	16.62
2.4	17.28	18.72
2.5	18.00	20.73
2.6	18.72	22.69
2.7	19.44	24.62
2.8	20.16	26.52
2.9	20.88	28.41
3.0	21.60	30.28

Table 5: Data for Speed Estimation Stage

Tip Speed Ratio λ	Rotating Speed ω	Captured Power
0.9	4.5	436.5
1.8	9.0	1487
2.7	13.5	2291
3.6	18.0	2561
4.5	22.5	2369
5.4	27.0	1881
6.3	31.5	1075

Data at other tidal current speeds can be generated with Eqns. (2.1)(2.2) and (2.3).

Training the neural networks is simple with the MATLAB function "fignet". There is also a function named "gensim" to convert the neural network function to a simulink block. This enables the neural networks to be embeded into the simulations.

Back-to-Back Converter Control

This back-to-back topology is widely used in distributed generations because of its flexibility. It connects the generator to the grid through a filter. The grid side converter maintains a constant DC link voltage and control the active power and the reactive power delivered to the grid. The machine side converter controls power generation, which is able to apply different control strategies. Control algorithms for the two converters are decoupled. In this paper, the machine side converter mainly controls the rotating speed of the turbine. Zero d-axis current control is applied to ensure a linear relation between electromagnetic torque and q-axis current for the PMSG [61]. Then the rotating speed is controlled by regulating the q-axis current. The control diagram is shown in Fig. 12. As noted above, the grid side converter is controlled to keep the DC-link voltage stable. A phase lock loop is used to obtain the angle of the grid voltage and to perform the park transformation. q-axis reference current is set to zero to eliminate reactive power.

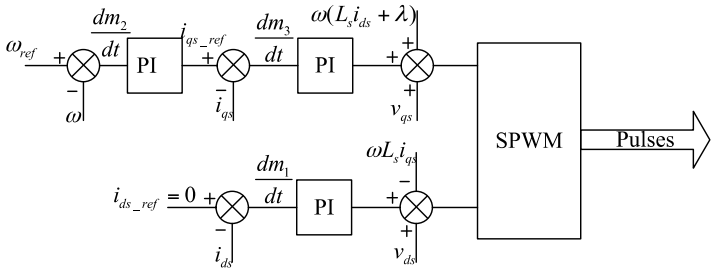

Figure 12: Control diagram of the machine side converter

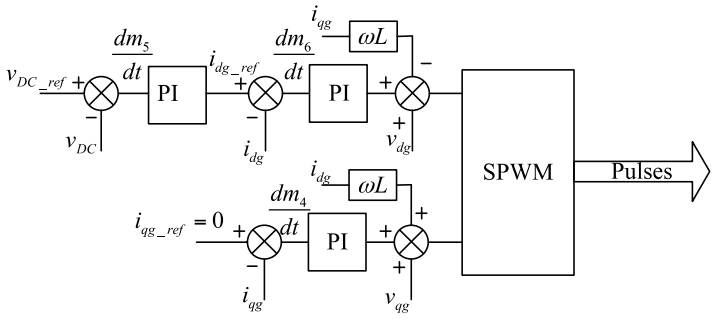

Figure 13: Control diagram of the grid side converter

The control diagram is shown in Fig. 13.

3.2.3 Modeling of the Controller

The model of the controllers for the machine side converter and the grid side converter are provided in this section. It is the basis for the small signal analysis in the next chapter.

The model of machine side converter with controller is

$$i_{ds}^* = 0 \tag{3.14}$$

$$\frac{dm_1}{dt} = i_{ds}^* - i_{ds} \tag{3.15}$$

$$v_{ds}^* = k_{P1}(i_{ds}^* - i_{ds}) + k_{I1}m_1 - p\omega L_s i_{qs} + R_s i_{ds} \tag{3.16}$$

$$\frac{dm_2}{dt} = \omega^* - \omega \tag{3.17}$$

$$\omega^* = g(v) \tag{3.18}$$

$$i_{qs}^* = k_{P2}(\omega^* - \omega) + k_{I2}m_2 \tag{3.19}$$

$$\frac{dm_3}{dt} = i_{qs}^* - i_{qs} \tag{3.20}$$

$$v_{qs}^* = k_{P3}(i_{qs}^* - i_{qs}) + k_{I3}m_3 + R_s i_{qs} + p\omega L_s i_{ds} + p\omega\psi_m, \tag{3.21}$$

where $g(v)$ is a function of v, realized by a neural network.

The model of the grid side converter with controller is

$$i_{qg}^* = 0 \tag{3.22}$$

$$\frac{dm_4}{dt} = i_{qg}^* - i_{qg} \tag{3.23}$$

$$u_{qg}^* = k_{P4}(i_{qg}^* - i_{qg}) + k_{I4}m_4 + \omega L_g i_{dg} + v_{qg} \tag{3.24}$$

$$\frac{dm_5}{dt} = v_{DC}^* - v_{DC} \tag{3.25}$$

$$i_{qg}^* = k_{P5}(v_{DC}^* - v_{DC}) + k_{I5}m_5 \tag{3.26}$$

$$\frac{dm_6}{dt} = i_{dg}^* - i_{dg} \tag{3.27}$$

$$u_{dg}^* = k_{P6}(i_{dg}^* - i_{dg}) + k_{I6}m_6 - \omega L_g i_{qg} + v_{dg}. \tag{3.28}$$

In the equations above, m_1 to m_6 are variables in the controllers, shown in Fig. 12

and Fig. 13.

3.3 Summary

This chapter is the most critical in this thesis, providing torque analysis and explaining the proposed control strategy.

The mechanical torque and electromagnetic torque are both important to the lifespan of the system. But electromagnetic torque is more critical due to the high moment of inertia of the turbine, and its fluctuation. As the mechanical torque and the electromagnetic torque are almost the same in steady state, they can both be regulated by controlling the electromagnetic torque. In this thesis, the torques are regulated by the rotating speed control.

Chapter 4

Small Signal Analysis

Stability is essential for the system. All parameters in the system, as well as operating conditions, have impacts on the stability. There are empirical ways to tune parameters to make the system stable. But this approach usually takes a long time and requires experience. Small signal analysis is another way to find the control parameters to make the system stable. On the other hand, small signal analysis can obtain the sensitivities of the system performance to the control parameters.

In this chapter, small signal analysis is performed to study the sensitivity of lifespan of tidal system to control parameters. This chapter provides eigenvalues and corresponding participation factors of the system. Impacts of control parameters to eigenvalues are also included.

4.1 Whole System Modeling

The models of all components of the system are provided in Chapter 2 and Chapter 3. The form of the whole model is

$$\dot{\mathbf{x}} = f(\mathbf{x}, \mathbf{u}), \tag{4.1}$$

where $\mathbf{x}$ is a column of state variables and $\mathbf{u}$ is a column of input variables.

The state variables are

$$\mathbf{x}^\top = \begin{bmatrix} \omega & i_{ds} & i_{qs} & m_1 & m_2 & m_3 & m_4 & m_5 & m_6 & i_{dg} & i_{qg} & v_{DC} \end{bmatrix} \tag{4.2}$$

After rearrangements, the following equations are derived.

$$\frac{d\omega}{dt} = \frac{\rho\pi R^3 v^2 C_p(\lambda)/\lambda + 3p\psi_m i_{qs}}{2J}, \tag{4.3}$$

derived from (2.1)(2.2)(2.3)(2.4)(2.8)(2.9).

$$\frac{di_{ds}}{dt} = \frac{-k_{P1} i_{ds} + k_{I1} m_1}{L_d}, \tag{4.4}$$

derived from (2.5)(3.14)(3.15)(3.16).

$$\frac{di_{qs}}{dt} = \frac{k_{P3}k_{P2}\omega^*(v) - k_{P3}k_{P2}\omega - k_{P3}k_{I2}m_2 + k_{I3}m_3}{L_q}, \tag{4.5}$$

derived from (2.6)(3.17)(3.18)(3.19)(3.20)(3.21).

$$\frac{dm_1}{dt} = -i_{ds}, \tag{4.6}$$

derived from (3.14)(3.15).

$$\frac{dm_2}{dt} = \omega^* - \omega, \tag{4.7}$$

which is the same as (3.17).

$$\frac{dm_3}{dt} = k_{P2}(\omega^* - \omega) + k_{I2}m_2 - i_{qs}, \tag{4.8}$$

derived from (3.17)(3.18)(3.19)(3.20).

$$\frac{dm_4}{dt} = -i_{qs}, \tag{4.9}$$

derived from (3.22)(3.23).

$$\frac{dm_5}{dt} = -v^*_{DC} + v_{DC}, \tag{4.10}$$

which is the same as (3.25).

$$\frac{dm_6}{dt} = k_{P5}(-v^*_{DC} + v_{DC}) + k_{I5}m_5 - i_{dg}, \tag{4.11}$$

derived from (3.25)(3.26)(3.27).

$$\frac{di_{dg}}{dt} = \frac{k_{P6}k_{P5}(-v^*_{DC} + v_{DC}) + k_{P6}k_{I5}m_5 - k_{P6}i_{dg} + k_{I6}m_6}{L_g}, \tag{4.12}$$

derived from (2.12)(3.25)(3.26)(3.27)(3.28).

$$\frac{di_{qg}}{dt} = \frac{-k_{P4}i_{qg} + k_{I4}m_4}{L_g}, \tag{4.13}$$

derived from (2.13)(3.22)(3.23)(3.24)

$$\frac{dv_{DC}}{dt} = -\frac{3(v_{ds}i_{ds} + v_{qs}i_{qs} + v_{dg}i_{dg})}{2Cv_{DC}}, \tag{4.14}$$

where

$$v_{ds}i_{ds} = (R_s - k_{P1})i_{ds}^2 + (k_{I1}m_1 - p\omega L_d i_{qs})i_{ds} \tag{4.15}$$

$$v_{qs}i_{qs} = (R_s - k_{P3})i_{qs}^2 + (k_{P3}k_{P2}(\omega^* - \omega) + k_{P3}k_{I2}m_2 + k_{I3}m_3 + p\omega L_q i_{ds} + p\omega\psi_m)i_{qs} \tag{4.16}$$

Eqn. (4.14) is rearranged from Eqn. (2.16). Eqn. (4.15) is derived from (3.16) and Eqn. (4.16) is derived from (3.21).

4.2 Linearization

It is difficult to analyze the nonlinear equations listed in the previous section. Linearization at an operating point is an approach to cope with nonlinearity. The form of the system model after linearization is

$$\mathbf{\Delta\dot{x}} = \mathbf{A\Delta x} + \mathbf{B\Delta u}, \tag{4.17}$$

where

$$\mathbf{A} = \begin{bmatrix} \frac{\partial f_1}{\partial x_1} & \frac{\partial f_1}{\partial x_2} & \cdots & \frac{\partial f_1}{\partial x_n} \\ \frac{\partial f_2}{\partial x_1} & \frac{\partial f_2}{\partial x_2} & \cdots & \frac{\partial f_2}{\partial x_n} \\ \vdots & \vdots & \ddots & \vdots \\ \frac{\partial f_n}{\partial x_1} & \frac{\partial f_n}{\partial x_2} & \cdots & \frac{\partial f_n}{\partial x_n} \end{bmatrix}, \tag{4.18}$$

and

$$\mathbf{B} = \begin{bmatrix} \frac{\partial f_1}{\partial u_1} & \frac{\partial f_1}{\partial u_2} & \cdots & \frac{\partial f_1}{\partial u_n} \\ \frac{\partial f_2}{\partial u_1} & \frac{\partial f_2}{\partial u_2} & \cdots & \frac{\partial f_2}{\partial u_n} \\ \vdots & \vdots & \ddots & \vdots \\ \frac{\partial f_n}{\partial u_1} & \frac{\partial f_n}{\partial u_2} & \cdots & \frac{\partial f_n}{\partial u_n} \end{bmatrix}. \tag{4.19}$$

In stability analysis, only **A** will be used. Thus the rest of this section is to calculate **A**. The subscript "0" means static operating point. The superscript "*" means reference. From Eqn. (4.18), the following matrix is obtained.

$$\mathbf{A} = \begin{bmatrix} a_{11} & & a_{13} & & & & & & & & & & \\ & a_{22} & & a_{24} & & & & & & & & & \\ a_{31} & a_{32} & & & a_{35} & a_{36} & & & & & & & \\ & a_{42} & & & & & & & & & & & \\ a_{51} & & & & & & & & & & & & \\ a_{61} & & a_{63} & & a_{65} & & & & & & & & \\ & & & & & & & & & a_{711} & & & \\ & & & & & & & & & & & a_{812} & \\ & & & & & & & a_{98} & & a_{910} & & a_{912} & \\ & & & & & & & a_{108} & a_{109} & a_{1010} & & a_{1012} & \\ & & & & & & a_{117} & & & & a_{1111} & & \\ a_{121} & a_{122} & a_{123} & a_{124} & a_{125} & a_{126} & & & & a_{1210} & & a_{1212} & \end{bmatrix}. \tag{4.20}$$

The elements in the matrix are listed in Table 6.

Table 6: Elements in **A** matrix

Element	Expression	Element	Expression
a_{22}	$-\frac{k_{P1}}{L_s}$	a_{11}	$\frac{\rho\pi R^3 v_0^2}{2J\lambda_0\omega_0}(-0.002464\lambda_0^5+0.036\lambda_0^4-0.1722\lambda_0^3+0.2383\lambda_0^2-0.0112)$
a_{24}	$\frac{k_{I1}}{L_s}$	a_{13}	$\frac{3p\psi_m}{2J}$
a_{31}	$-\frac{k_{P2}k_{P3}}{L_s}$	a_{108}	$\frac{k_{P6}k_{I5}}{L_g}$
a_{32}	$-\frac{k_{P3}}{L_s}$	a_{109}	$\frac{k_{I6}}{L_g}$
a_{35}	$\frac{k_{I2}k_{P3}}{L_s}$	a_{1010}	$-\frac{k_{P6}}{L_g}$
a_{36}	$\frac{k_{I3}}{L_s}$	a_{1012}	$\frac{k_{P5}k_{P6}}{L_g}$
a_{42}	-1	a_{117}	$\frac{k_{I4}}{L_g}$
a_{51}	-1	a_{1111}	$-\frac{k_{P4}}{L_g}$
a_{61}	$-k_{P2}$	a_{121}	$\frac{3i_{qs0}}{3Cv_{DC0}}(k_{P2}k_{P3}-p\psi_m)$
a_{63}	-1	a_{122}	$-\frac{3k_{I1}m_{10}}{3Cv_{DC0}}+\frac{3i_{ds0}}{Cv_{DC0}}(k_{P1}-R_s)$
a_{65}	k_{I2}	a_{123}	$-\frac{3}{2Cv_{DC0}}(k_{P2}k_{P3}\omega_0^*-k_{P2}k_{P3}\omega_0+k_{I2}k_{P3}m_{20}+k_{I3}m_{30}+p\omega_0\psi_m)$
a_{711}	-1	a_{124}	$-\frac{3k_{I1}i_{ds0}}{2Cv_{DC0}}$
a_{812}	1	a_{125}	$\frac{3k_{I2}k_{P3}i_{qs0}}{2Cv_{DC0}}$
a_{98}	k_{I5}	a_{126}	$\frac{3k_{I3}i_{qs0}}{2Cv_{DC0}}$
a_{910}	-1	a_{1210}	$-\frac{3v_{dg}}{2Cv_{DC0}}$
a_{912}	k_{P5}	a_{1212}	$\frac{3}{2Cv_{DC0}^2}((R_s-k_{P1})i_{ds0}^2+k_{I1}m_{10}i_{ds0}+(R_s-k_{P3})i_{qs0}^2$ $+(k_{P3}k_{P2}(\omega_0^*-\omega_0)+k_{P3}k_{I2}m_{20}+k_{I3}m_{30}+p\omega_0\psi_m)i_{qs0}+v_{dg}i_{dg0})$

4.3 Eigenvalues and Participation Factors

Eigenvalues of matrix **A** determine the performance of the system. Participation factors show the relation between an eigenvalue and a state variable.

An eigenvalue λ of a matrix **A** satisfies the conditon that

$$\mathbf{A}\phi = \lambda\phi, \tag{4.21}$$

where ϕ is the eigenvector corresponding to λ.

A right eigenvector is a column vector that satisfies

$$\mathbf{A}\phi_i = \lambda_i\phi_i, \tag{4.22}$$

and a left eigenvector is a row vector that satisfies

$$\psi_i\mathbf{A} = \lambda_i\psi_i. \tag{4.23}$$

Define

$$\mathbf{\Phi} = \begin{bmatrix} \phi_1 & \phi_2 & \cdots & \phi_n \end{bmatrix}, \tag{4.24}$$

and

$$\mathbf{\Psi} = \begin{bmatrix} \psi_1 \\ \psi_2 \\ \vdots \\ \psi_n \end{bmatrix}. \tag{4.25}$$

Define the participation factor matrix

$$\mathbf{P} = \begin{bmatrix} \mathbf{p_1} & \mathbf{p_2} & \cdots & \mathbf{p_n} \end{bmatrix}, \tag{4.26}$$

where

$$\mathbf{p_i} = \begin{bmatrix} p_{1i} \\ p_{2i} \\ \vdots \\ p_{ni} \end{bmatrix} = \begin{bmatrix} \phi_{1i}\psi_{i1} \\ \phi_{2i}\psi_{i2} \\ \vdots \\ \phi_{ni}\psi_{in} \end{bmatrix}. \tag{4.27}$$

The parameters used in the small signal analysis are listed in Table 7. Jian and Taofeek contributed a lot to obtain the appropriate parameters. The eigenvalues and participation factors are listed in Table 8.

Table 7: Parameters for Small Signal Analysis

Parameter	Value
Number of pole pairs (p)	24
Stator resistance (R_s)	3.53
Stator d-axis inductance (L_d)	0.0782
Stator q-axis inductance (L_q)	0.0782
Flux (ψ_m)	0.91781
Combined moment of inertia (J)	6.61
Grid side filter inductance (L_g)	1×10^{-3}
Radius of turbine (R)	0.5
Water density (ρ)	1025
Grid d-axis voltage (v_{dg})	208
DC link voltage reference (v^*_{DC})	1000
kp1 (i_{ds})	100
ki1 (i_{ds})	3
kp2 (ω)	10
ki2 (ω)	5
kp3 (i_{qs})	500
ki3 (i_{qs})	3
kp4 (i_{qg})	400
ki4 (i_{qg})	2
kp5 (v_{DC})	0.1
ki5 (v_{DC})	40
kp6 (i_{dg})	400
ki6 (i_{dg})	2

Table 8: Eigenvalues and Participation Factors

λ	Eigenvalues	Associate Variable 1	Participation Factor 1	Associate Variable 2	Participation Factor 2
λ_1	-6×10^{-3}	m_3	1		
λ_2	-5×10^{-3}	m_4	1		
λ_3	-5×10^{-3}	m_6	1		
λ_4	-3×10^{-2}	m_1	1		
λ_5	-0.49	m_2	1		
λ_6	$-8.8 + 111i$	m_5	0.5	v_{DC}	0.5
λ_7	$-8.8 - 111i$	m_5	0.5	v_{DC}	0.5
λ_8	-51	ω	1		
λ_9	-1.3×10^3	i_{ds}	1		
λ_{10}	-6.3×10^3	i_{qs}	1		
λ_{11}	-4.0×10^5	i_{dg}	1		
λ_{12}	-4.0×10^5	i_{qg}	1		

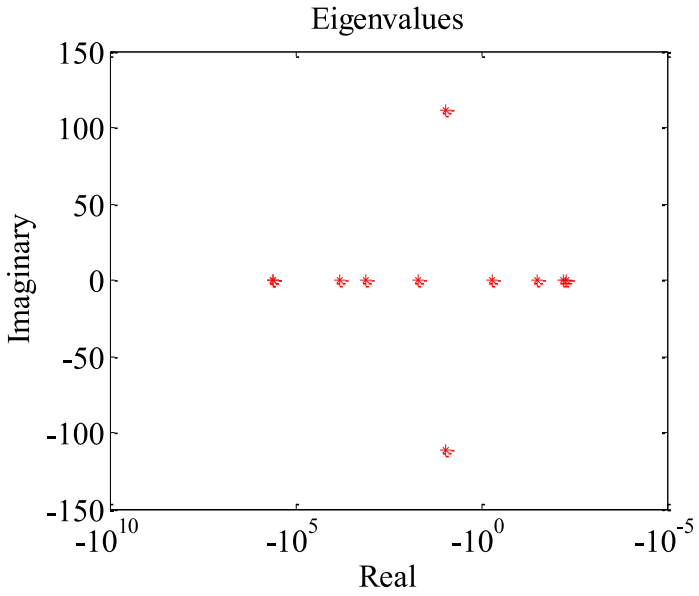

Figure 14: Eigenvalues

All eigenvalues have negative real parts, which means the system is stable. ω and $\imath_{qs}$ are the variables most related to mechanical torque and electromagnetic torque, therefore contribute most to the lifespan of the tidal system. According to the table, these two variables participate most in eigenvalues λ_8 and λ_{10}. So we can study the sensitivity of λ_8 and λ_{10} to the control parameters.

4.4 Eigenvalue Trajectories

This section studies how the control parameters influence the performance of the system from eigenvalue trajectories. The graph of all 12 eigenvalues is provided first. Then the eigenvalue trajectories under different conditions are listed.

The eigenvalues of the system at tidal current speed $v = 2.5$ m/s is shown in Fig. 14. All plots in this section are semi-log graphs. The system is stable because all eigenvalues have negative real parts.

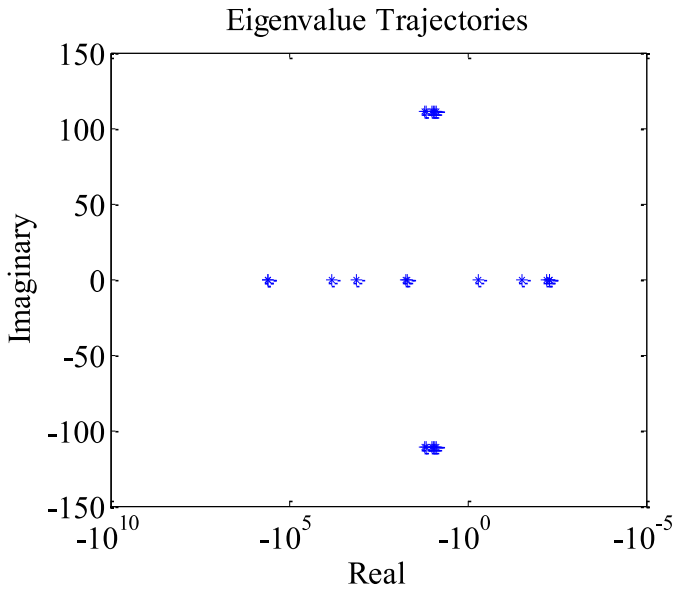

Figure 15: Eigenvalue trajectories with tidal current speed variation

The eigenvalue trajectories with tidal current speed variation is shown in Fig. 15. The system is stable at all tidal current speeds from 0m/s to 3.6m/s. The rest of this section provides eigenvalue trajectories under control parameters change.

Fig. 16 shows the eigenvalue trajectories when k_{P1} varies from 60 to 150 (left) and k_{I1} varies from 2 to 3.8 (right). They causes significant changes in λ_4 and λ_9, corresponding to dynamics in m_1 and i_{ds}, which matches the control diagram.

Fig. 17 shows the eigenvalue trajectories when k_{P2} varies from 1 to 19 (left) and k_{I2} varies from 1 to 10 (right). λ_5 corresponds to m_2 while λ_8 corresponds to ω. As ω has an direct impact on the electromagnetic torque, the farther λ_8 is from the imaginary axis, the better. However, a greater k_{P2} makes λ_5 closer to the imaginary axis. In this case, simulations can help select the parameters.

Fig. 18 shows the eigenvalue trajectories when k_{P3} varies from 400 to 580 (left) and k_{I3} varies from 2 to 3.8 (right). The change in k_{P3} causes λ_1, λ_6, λ_7 and λ_{10} to move.

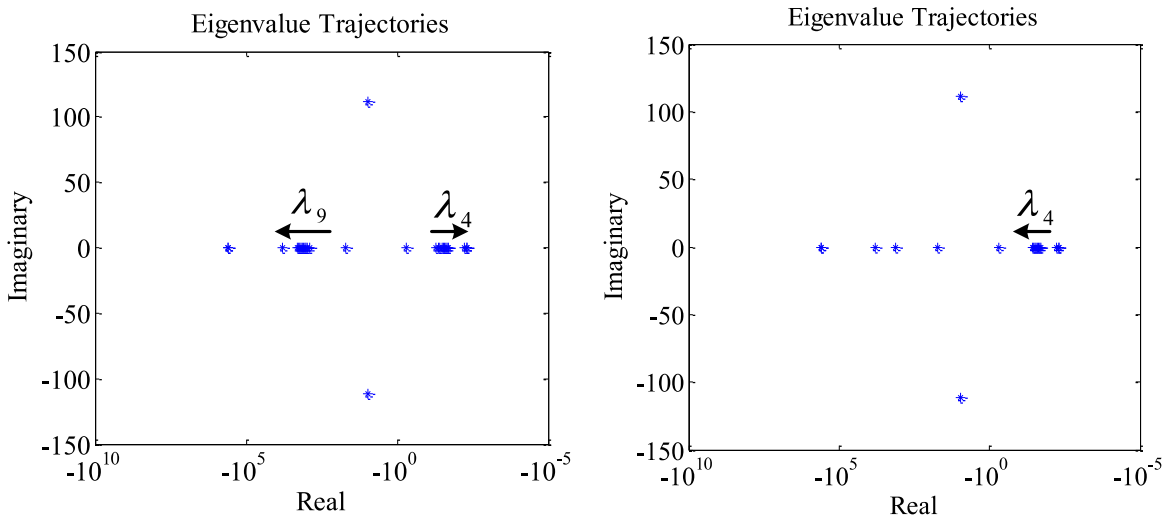

Figure 16: Eigenvalue trajectories with variations of k_{P1} and k_{I1}

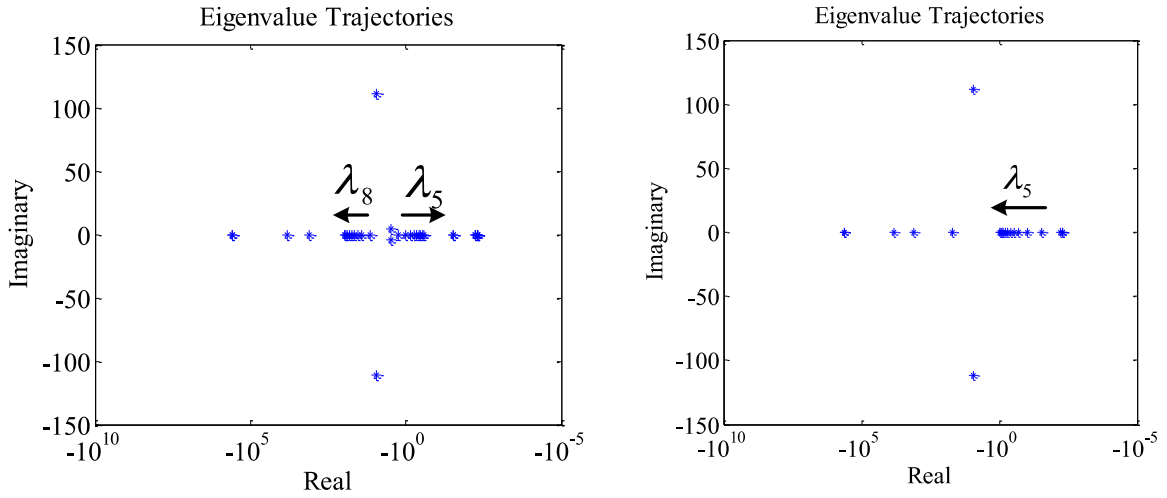

Figure 17: Eigenvalue trajectories with variations of k_{P2} and k_{I2}

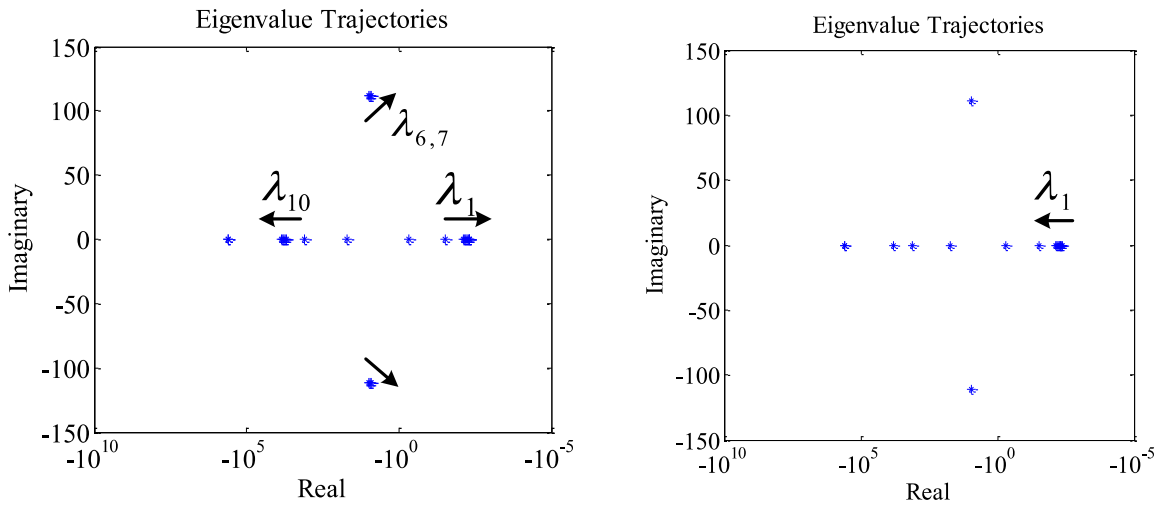

Figure 18: Eigenvalue trajectories with variations of k_{P3} and k_{I3}

λ_1 corresponds to m_3 and λ_{10} corresponds to i_{qs}, which is related to the electromagnetic torque. Similar to the previous case, k_{P3} should be great enough without losing stability. The trajectories of λ_6 and λ_7 show that k_{P3} also affects the dynamics in the DC link voltage.

Fig. 19 shows the eigenvalue trajectories when k_{P4} varies from 300 to 480 (left) and k_{I4} varies from 1 to 2.8 (right). λ_2 and λ_{12} correspond to m_4 and i_{qg}, respectively. This affects the quality of the output currents to the grid.

Fig. 20 shows the eigenvalue trajectories when k_{P5} varies from 0.05 to 0.14 (left) and k_{I5} varies from 30 to 48 (right). λ_6 and λ_7 correspond to m_5 and v_{DC}. We can apply a greater k_{P5} and a smaller k_{I5} to improve the performance of v_{DC}.

Fig. 21 shows the eigenvalue trajectories when k_{P6} varies from 300 to 480 (left) and k_{I6} varies from 1 to 2.8 (right). λ_3 and λ_{11} correspond to m_6 and i_{dg}. Selection of k_{P6} and k_{I6} affects the quality of output currents to the grid.

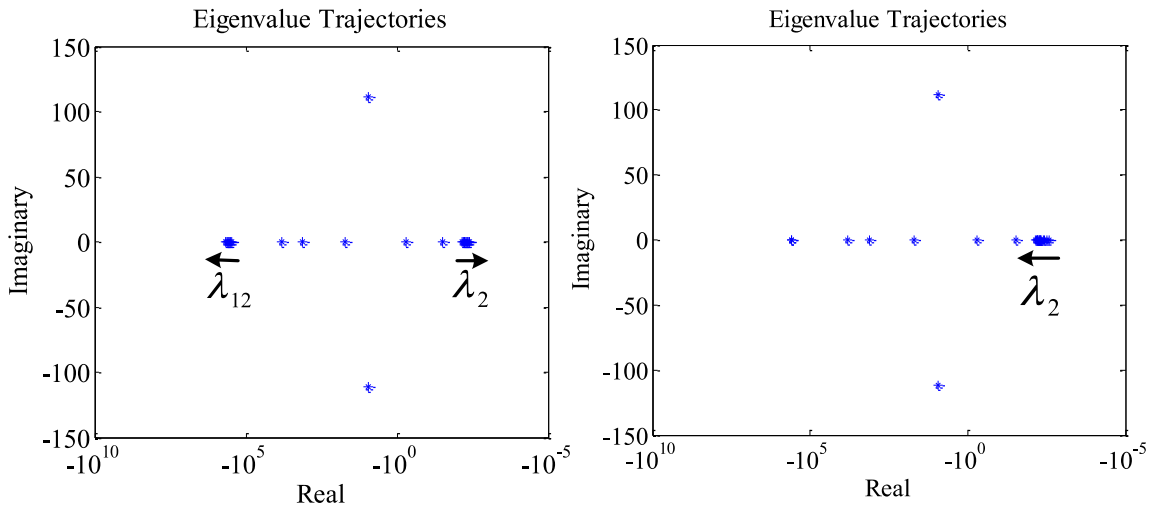

Figure 19: Eigenvalue trajectories with variations of k_{P4} and k_{I4}

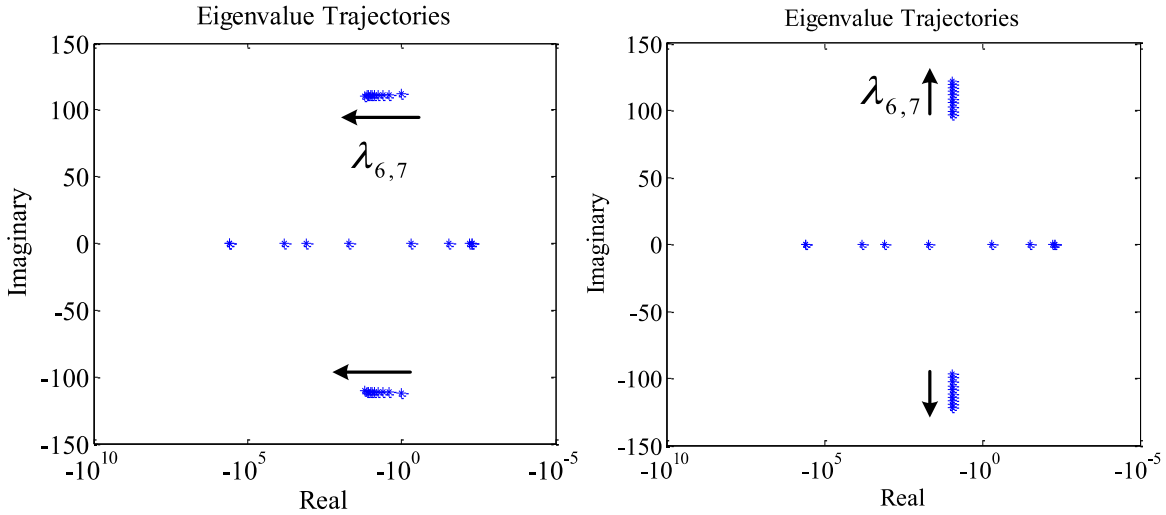

Figure 20: Eigenvalue trajectories with variations of k_{P5} and k_{I5}

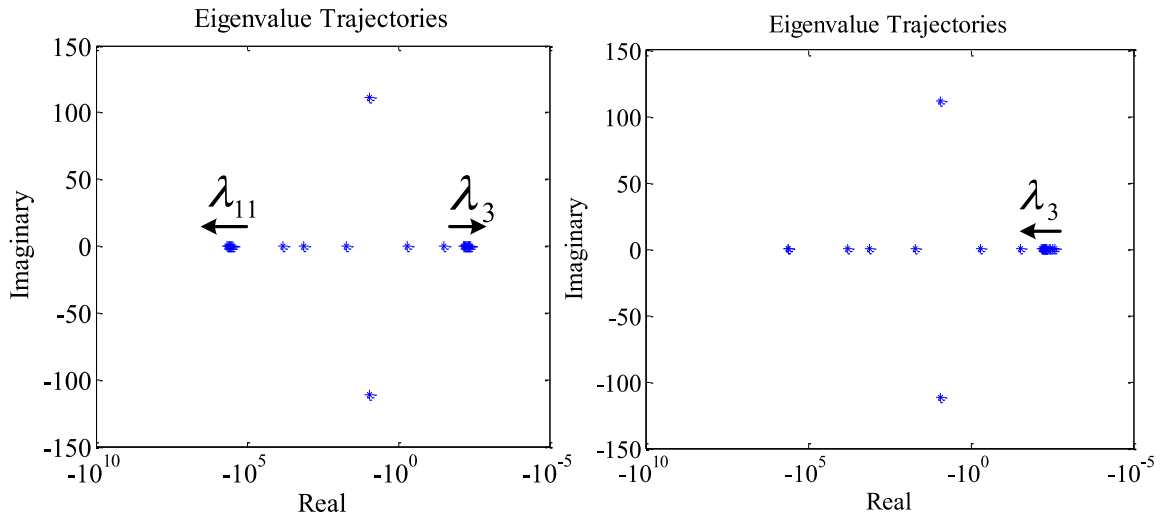

Figure 21: Eigenvalue trajectories with variations of k_{P6} and k_{I6}

4.5 Summary

This chapter performs the small signal analysis for the tidal system.

Based on the models for all components in previous chapters, this chapter derives the model for the whole system. After linearization, the characteristic matrix is obtained and eigenvalues are calculated, demonstrating the stability of this system. Finally, the eigenvalue trajectories under different conditions are provided and analyzed. The control parameters k_{P2} and k_{P3} have the most significant impacts on the mechanical torque and electromagnetic torque, and should be studied in simulations.

Chapter 5

Simulations

This chapter provides simulation results [1] to validate the proposed control strategy, and the small signal analysis in Chapter 4. Before the simulation results, the real time simulator is introduced.

5.1 Simulation Techniques

In this research, a real time simulator was used to perform simulations. This simulator, with multiple CPUs and huge memory, is able to run simulations in real time and store large amounts of data in it. The software interface is RT-Lab. RT-Lab is responsible for generating C code from the modified SimPowerSystem model, for transferring the C code to the simulator, for receiving the compiled files, for sending out compiled files to execute, for interaction with the simulator during simulations, and for receiving simulation results. The real time simulator is controlled by RT-Lab, and is responsible for compilation, simulation, and results extraction. This process is shown in Fig. 22. Multiple subsystems, including one master subsystem and multiple slave subsystems, can be run on different CPUs in the simulator.

Speed and accuracy are the most important indices for simulations. Generally, accuracy is dependent on the time step, and time step determines simulation speed. The

[1] The author thanks Taofeek Orekan and Jian Zhang for their tremendous contributions to the numerical results in this chaper.

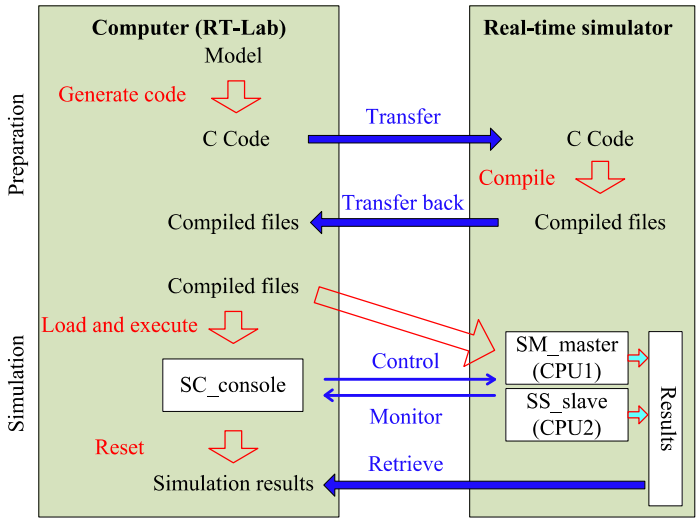

Figure 22: Real time simulator simulation structure

reason is as follows.

An electrical system is described with differential and algebraic equations (DAEs). To solve the differential equations with computers, numerical integrations must be performed in all types of solvers, which introduce errors. One approach to reduce integration error is using a small time step. In real-time simulations, fixed-step is required due to synchronization with real time. Using a small time step in the whole simulation makes it slow. In PSCAD, trapezoidal integration method is used, which is 2nd order. In this research, Artemis (Advanced real-time electromechanical simulator), a simulator with 5th order integration method is used. It is able to get as accurate results as 2nd order integration with a $10\mu s$ time step, with a $100\mu s$ time step. Thus the simulation speed is improved considerably without losing intolerable accuracy.

The simulation structure for the tidal system is shown in Fig. 23. "SM_system" and "SS_control" are two subsystems that will be assigned to two CPUs in the simulator. There is also one subsystem "SC_console" runing on a computer for monitoring.

A 12-hour simulation was carried out with real data in Fig. 2 as input. The advantage

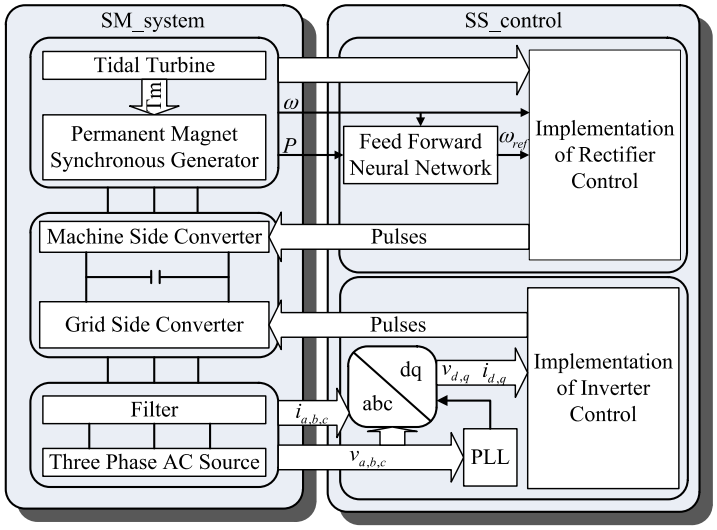

Figure 23: Simulation structure of the tidal system

of real-time simulation is obvious in this case. Simulation in Simulink would become prohibitively slow as data accumulate in its memory.

There are still other issues when simulations are performed. The tidal current speed is recorded every 6 minutes, but the simulation time step is 4 microseconds. Holding one value for 6 minutes does not fit real conditions, where tidal current speeds vary continuously with time. Linear interpolation was used to solve this issue in a simple way. The simulation results include 1.08×10^{10} double data per variable. If ten variables are monitored, the results will take up 100 GB. The real time simulator is able to store such data with its huge memory. But it is very difficult to deal with these data with Matlab. Still, it is unnecessary. Our method is to sample one point every 10000 points. This considerably reduces the amount of data to be processed, and improves efficiency.

The top level and the SM_system subsystem of the simulation model are shown in Fig. 24 and Fig. 25.

In the rest of this chapter, different cases will be studied and discussed. First, the real tidal current speed data will be used to test system performance under normal

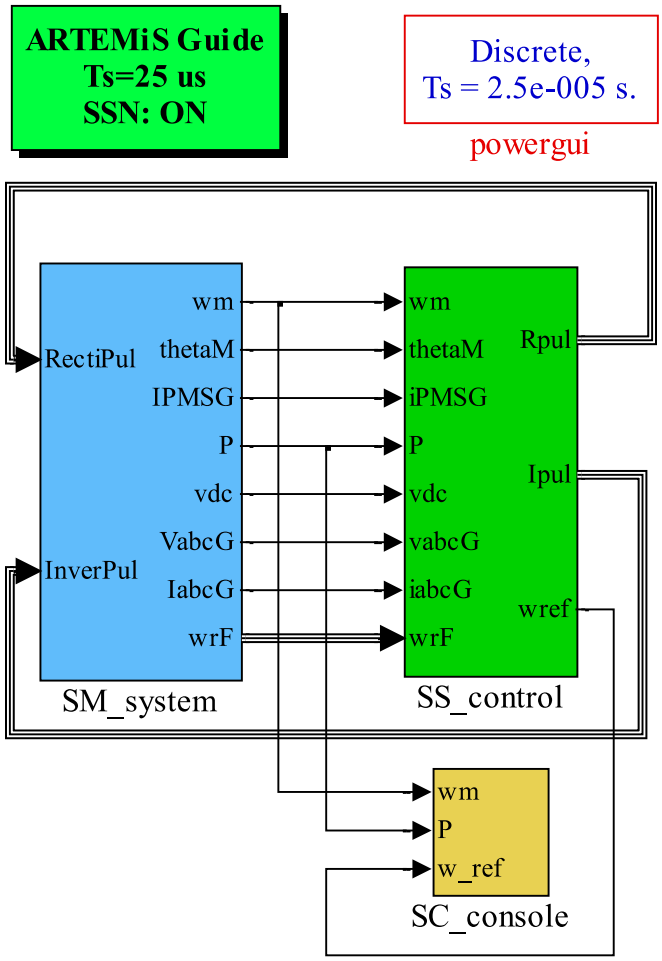

Figure 24: Top level of the tidal system

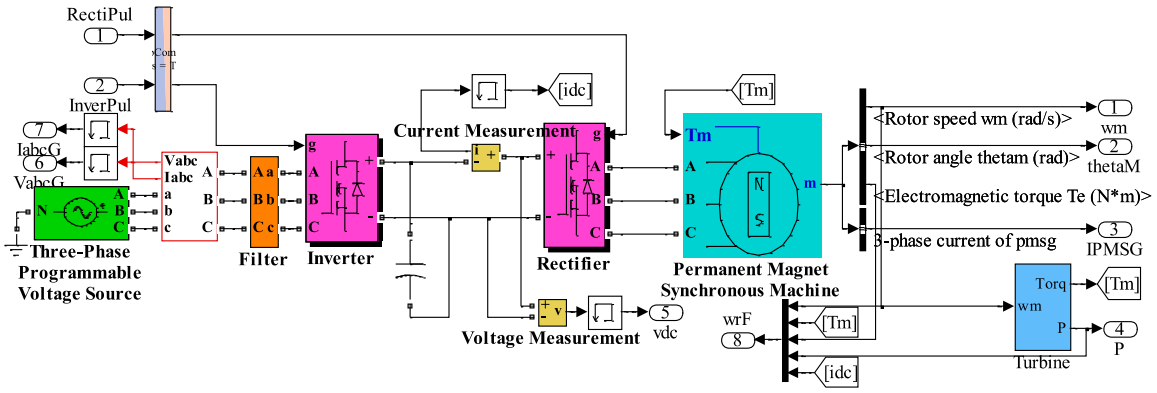

Figure 25: SM_system subsystem of the tidal system

conditions. Then, simulations under step-up tidal current speed are performed to test the performance under various frequency components.

5.2 Simulation Results

5.2.1 Indices Definition

Mechanical torque, electromagnetic torque, captured power and damage caused by the torque are the main indices to be compared in the following simulations. The first three are obtained directly from simulations, and damage is calculated with Miners rule

$$D = \Sigma \frac{n_i}{N_{fi}}, \tag{5.1}$$

where n_i is the number of cycles at a certain torque and N_{fi} is number of cycles to failure at the torque calculated with (3.1). Rainflow counting method [62] is used to count cycles in the simulations. Note that this is only a statistically estimation of failure caused by stress. In reality, other factors such as corrosion will result in a shorter life. That part is out of the scope of this thesis.

Table 9: Results for Case 1

	Mechanical Torque		Electromagnetic Torque		Energy
	Max(Nm)	D	Max(Nm)	D	(kWh)
MPP Control	170.62	4.05×10^{-5}	175.31	2.28×10^{-4}	7.71
Hybrid Control	127.72	2.29×10^{-7}	130.96	2.27×10^{-6}	7.60
%	74.85%	**0.57%**	74.70%	**1.00%**	98.48%

As is discussed in Chapter 3, life expenditure of shaft is calculated with electromagnetic torque, and that of turbine blades is calculated with mechanical torque.

5.2.2 Simulation Results and Discussions

Case 1: Normal condition with real tidal current data

Simulation was conducted with part of the data shown in Fig. 2 for 12 hours. Simulations are completed under the help of Taofeek and Jian. Maximum power point method and the proposed hybrid methods (in Fig. 8) were simulated and compared. Results are shown in Fig. 26.

At low tidal current speeds, the two strategies produce the same results. Red curves show the results for the maximum power point strategy. It captures more power, as is shown in the last trace, but endures higher mechanical torque and electromagnetic torque, shown in trace 2 and trace 3. The hybrid control strategy captures only a small amount less power than the maximum power point control, but reduces the torque, which leads to significant life extension. Comparison of the maximum power point control and the hybrid control is shown in Table 9.

The hybrid control strategy has 0.57% life expenditure of MPP control from mechanical torque, which means the life cycle of turbine blades will be extended for 176 times. Similarly, life cycle of the shaft will be extended for 100 times. The captured energy is almost the same.

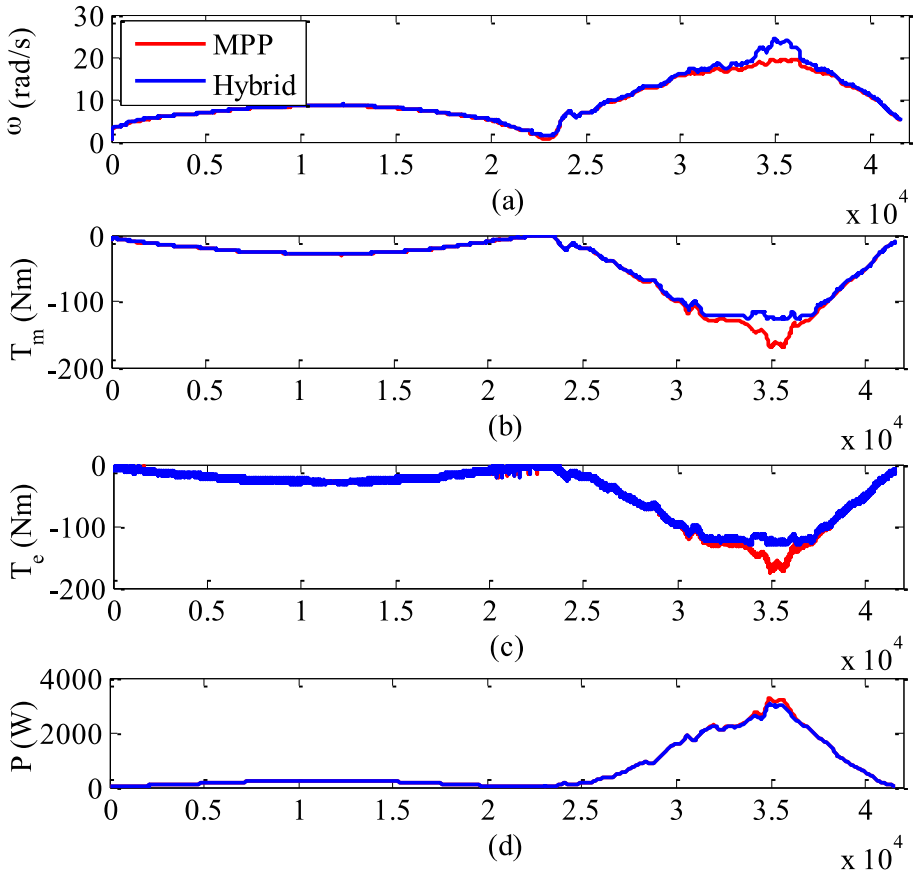

Figure 26: Simulation results for Case 1

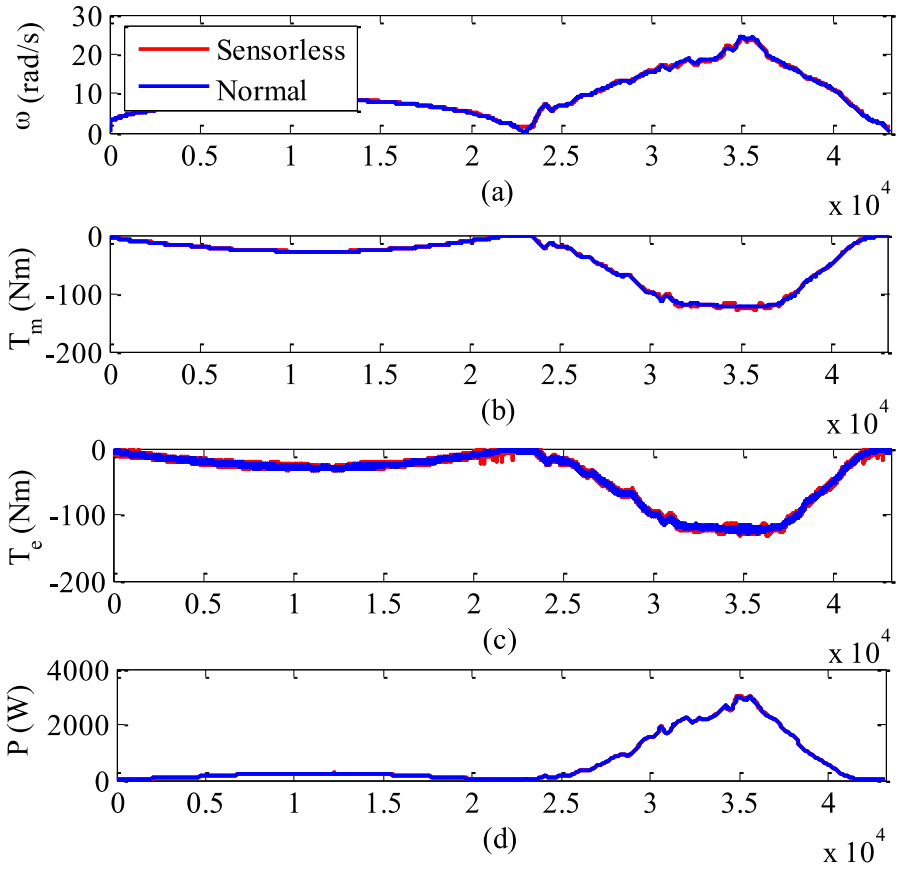

Figure 27: Simulation results for Case 2

Case 2: Effect of neural network

According to Chapter 3, it is mentioned that the neural network is used to estimate the tidal current speed. This is to enhance the reliability of the system by eliminating the speed sensor. However, the performance of the neural network is not perfect. This case is to study the effect of the neural network.

Similar to the previous case, a 12-hour simulation was performed. The simulation results are compared with the previous case, shown in Fig. 27.

The results without the speed estimation neural network is smoother. Quantitive comparisons can be found in Table 10. Several reasons can lead to the differences:

Table 10: Results for Case 2

	Mechanical Torque		Electromagnetic Torque		Energy
	Max(Nm)	D	Max(Nm)	D	(kWh)
With neural network	127.72	2.29×10^{-7}	130.96	2.27×10^{-6}	7.60
Without neural network	122.81	1.14×10^{-7}	128.25	1.60×10^{-6}	7.60
%	96.15%	**49.64%**	97.93%	**70.35%**	99.95%

- The neural network is not well trained;
- The tidal current speed signal from the sensor has noise and delay in real conditions, which are not included in the simulation;
- The measured tidal current speed may not be exactly the same as that at the turbine rotor.

Note that the tidal current speed sensor itself may fail in the harsh environment, which will lead to the malfunction of the control system. Consider all these factors, using the sensor to get the tidal current speed signal may not be a good idea.

Case 3: Effect of control parameter k_{P2}

According to Chapter 4, the control parameters that have the most significant impacts on the lifespan of the system are k_{P2} and k_{P3}.

In the previous case, normal condition, which is often the case, was simulated. However, sometimes there may be a gust, which causes unrecoverable damages. To study this extreme condition, a step-up tidal current speed was fed to the system. This also makes it possible to study system response to various frequencies. The tidal current speed steps from $v = 1$m/s to $v = 2.5$m/s at $t = 5$s. Simulation results are shown in Fig. 28. The red lines are results when k_{P2} is 10 while the blue dots are the resuts when k_{P2} is 12.

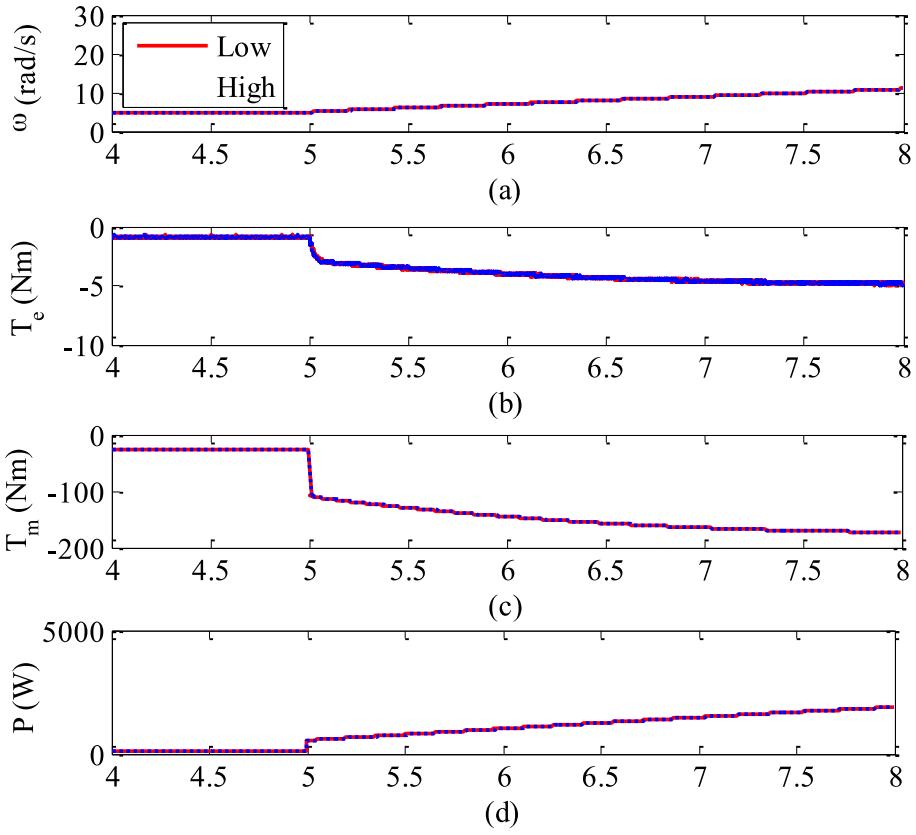

Figure 28: Simulation results for Case 3

Table 11: Results for Case 3

	Mechanical Torque		Electromagnetic Torque		Energy Captured
	Max(Nm)	D	Max(Nm)	D	(J)
$k_{P2} = 10$	127.95	2.28×10^{-6}	4.94	7.47×10^{-34}	3.87×10^{3}
$k_{P2} = 12$	127.96	2.29×10^{-6}	4.94	7.29×10^{-34}	3.86×10^{3}

Table 12: Results for Case 4

	Mechanical Torque		Electromagnetic Torque		Energy Captured
	Max(Nm)	D	Max(Nm)	D	(J)
$k_{P3} = 500$	127.95	2.28×10^{-6}	4.94	7.47×10^{-34}	3.87×10^{3}
$k_{P3} = 600$	127.95	2.28×10^{-6}	4.94	7.54×10^{-34}	3.87×10^{3}

The mechanical torque and the electromagnetic torque change significantly at $t = 5$s. The electromagnetic torque is far less than the mechanical torque because the rotor of the turbine is speeding up. The differences between the two conditions are not obvious through the figures, but slight differences can be seen in Table 11. A greater k_{P2} leads to a little higher damage and captured less power.

Case 4: Effect of control parameter k_{P3}

This section studies the effect of the control parameter k_{P3}. Same as the previous case, the tidal current speed steps from $v = 1$m/s to $v = 2.5$m/s at $t = 5$s. Simulation results are shown in Fig. 29. The red lines are results when k_{P3} is 500 while the blue dots are the resuts when k_{P3} is 600.

Still, the differences between the two conditions are not obvious through the figures, but slight differences can be seen in Table 12. A greater k_{P3} leads to a higher damage in terms of electromagnetic torque.

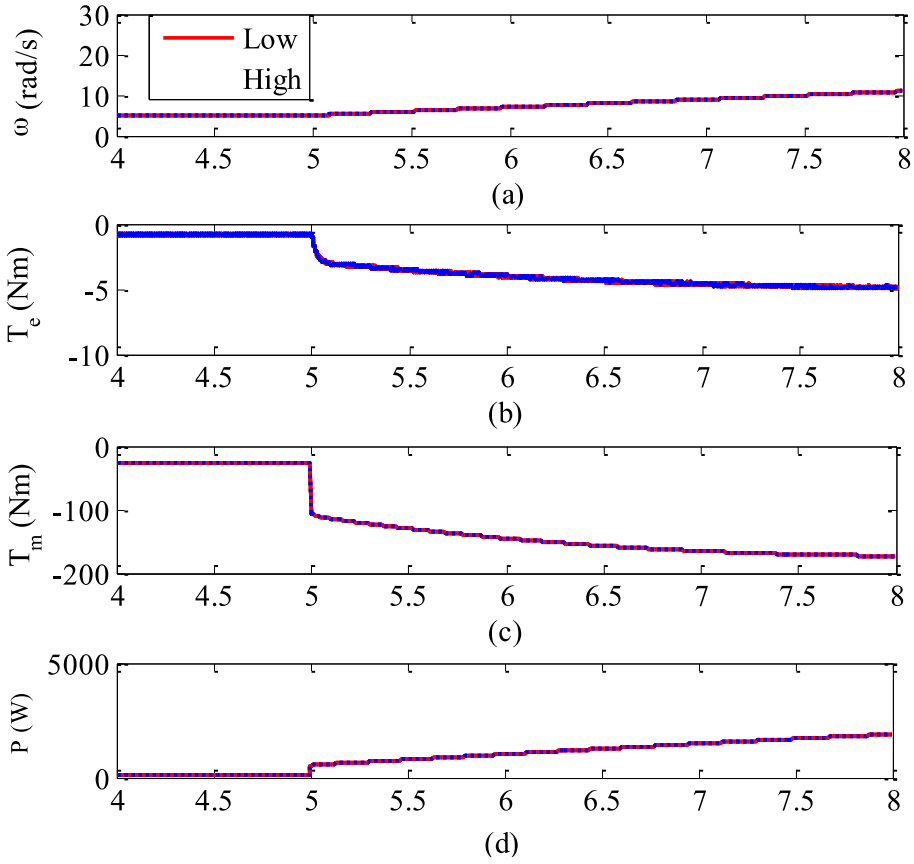

Figure 29: Simulation results for Case 4

5.3 Summary

This chapter introduces the simulation tool used in this research and provided simulation results. The first case shows that the proposed hybrid control strategy is able to extend the lifespan of the turbine system tens of times. The second case shows that the performance of the neural network is not good enough and leads to extra damage to the system. The last two cases study the impacts of control parameters.

Chapter 6

Conclusions

This thesis proposes a control strategy for a tidal current energy conversion system, and realizes it in a simulation model for validation.

This control strategy aims to extend the lifespan of the tidal system. From torque analysis, it is seen that the magnitude and the fluctuation of the mechanical torque and the electromagnetic torque cause damage to the turbine blades and the shaft. By reducing the torques, the stress will be significantly mitigated without losing much power.

This control strategy applies the maximum power point control at low tidal current speed range, and constant torque control at high tidal current speed range. This leads to the mitigation of the mechanical torque and electromagnetic torque. Neural network is used for tidal speed estimation and reference rotating speed generation.

Small signal analysis proves the stability of the designed system at a certain tidal current speed range. The eigenvalue trajectories demonstrate how the control parameters affect the system performance.

Simulation results are compared between maximum power point strategy and the proposed hybrid strategy through simulations. The life of turbine blades and shaft is extended significantly under the hybrid strategy at little cost of power.

Bibliography

[1] J. Heidemann, M. Stojanovic, and M. Zorzi, "Underwater sensor networks: applications, advances and challenges," *Philosophical Transactions of the Royal Society A: Mathematical, Physical and Engineering Sciences*, vol. 370, no. 1958, pp. 158–175, 2012.

[2] X. Xu, S. Zhou, K. Mahmood, L. Wei, and J.-H. Cui, "Study of class-D power amplifiers for underwater acoustic OFDM transmissions," in *Oceans - San Diego, 2013*, Sept 2013, pp. 1–3.

[3] J. O. Lamell, T. Trumbo, and T. F. Nestli, "Offshore platform powered with new electrical motor drive system," in *Petroleum and Chemical Industry Conference, 2005. Industry Applications Society 52nd Annual.* IEEE, 2005, pp. 259–266.

[4] X. Xu, Z. Wang, S. Zhou, and L. Wan, "Parameterizing both path amplitude and delay variations of underwater acoustic channels for block decoding of orthogonal frequency division multiplexing," *The Journal of the Acoustical Society of America*, vol. 131, no. 6, pp. 4672–4679, 2012.

[5] B. Li, S. Zhou, M. Stojanovic, L. Freitag, and P. Willett, "Multicarrier communication over underwater acoustic channels with nonuniform Doppler shifts," *Oceanic Engineering, IEEE Journal of*, vol. 33, no. 2, pp. 198–209, April 2008.

[6] X. Xu, E. Sang, N. Li, and G. Qiao, "Channel estimation algorithm in underwater acoustic communication based on DFT and OFDM," *Journal of Data Acquisition & Processing, China*, vol. 24, Jan. 2009.

[7] K. Tu, D. Fertonani, T. Duman, M. Stojanovic, J. Proakis, and P. Hursky, "Mitigation of intercarrier interference for ofdm over time-varying underwater acoustic channels," *Oceanic Engineering, IEEE Journal of*, vol. 36, no. 2, pp. 156–171, April 2011.

[8] X. Xu, G. Qiao, J. Su, P. Hu, and E. Sang, "Study on turbo code for multicarrier underwater acoustic communication," in *Wireless Communications, Networking and Mobile Computing, 2008. WiCOM'08. 4th International Conference on.* IEEE, 2008, pp. 1–4.

[9] E. Sang, X. Xu, G. Qiao, and J. Su, "Study on ZP-OFDM for underwater acoustic communication," in *Neural Networks and Signal Processing, 2008 International Conference on.* IEEE, 2008, pp. 299–302.

[10] J. Tao, Y. Zheng, C. Xiao, and T. Yang, "Robust MIMO underwater acoustic communications using turbo block decision-feedback equalization," *Oceanic Engineering, IEEE Journal of*, vol. 35, no. 4, pp. 948–960, Oct 2010.

[11] X. Xu, S. Zhou, A. K. Morozov, and J. C. Preisig, "Per-survivor processing for underwater acoustic communications with direct-sequence spread spectrum," *The Journal of the Acoustical Society of America*, vol. 133, no. 5, pp. 2746–2754, 2013.

[12] P. Carroll, S. Zhou, H. Zhou, X. Xu, J.-H. Cui, and P. Willett, "Underwater localization and tracking of physical systems," *Journal of Electrical and Computer Engineering*, vol. 2012, p. 2, 2012.

[13] J.-H. Cui, J. Kong, M. Gerla, and S. Zhou, "The challenges of building mobile underwater wireless networks for aquatic applications," *Network, IEEE*, vol. 20, no. 3, pp. 12–18, May 2006.

[14] I. F. Akyildiz, D. Pompili, and T. Melodia, "Underwater acoustic sensor networks: research challenges," *Ad hoc networks*, vol. 3, no. 3, pp. 257–279, 2005.

[15] T. Lewis, "The status of ocean energy development in europe and some current research questions," in *OCEANS 2011*. IEEE, 2011, pp. 1–6.

[16] P. Yuan, S. Wang, H. Shi, P. Guo, and Z. Dong, "Overview and proposal for development of ocean energy test sites in china," in *OCEANS, 2012 - Yeosu*, May 2012, pp. 1–6.

[17] S. D. Hicks and M. W. Szabados, *Understanding tides*. US Department of Commerce, National Oceanic and Atmospheric Administration, National Ocean Service, 2006.

[18] T. J. Hammons, "Tidal power," *Proceedings of the IEEE*, vol. 81, no. 3, pp. 419–433, 1993.

[19] A. Muetze and J. Vining, "Ocean wave energy conversion-a survey," in *Industry Applications Conference, 2006. 41st IAS Annual Meeting. Conference Record of the 2006 IEEE*, vol. 3. IEEE, 2006, pp. 1410–1417.

[20] (2010, Aug.) The world offshore renewable energy report 2004-2008. [Online]. Available: http://www.ppaenergy.co.uk/web-resources/resources/356866df2d2.pdf

[21] I. Bryden and G. Melville, "Choosing and evaluating sites for tidal current development," *Proceedings of the Institution of Mechanical Engineers, Part A: Journal of Power and Energy*, vol. 218, no. 8, pp. 567–577, 2004.

[22] F. O Rourke, F. Boyle, and A. Reynolds, "Tidal energy update 2009," *Applied Energy*, vol. 87, no. 2, pp. 398–409, 2010.

[23] Marine current turbines. [Online]. Available: http://www.marineturbines.com/

[24] IT power. [Online]. Available: http://www.itpower.co.uk/

[25] Verdant power. [Online]. Available: http://www.verdantpower.com/

[26] Open hydro. [Online]. Available: http://www.openhydro.com/

[27] Clean current. [Online]. Available: http://www.cleancurrent.com/tidal-turbines

[28] M. Esteban and D. Leary, "Current developments and future prospects of offshore wind and ocean energy," *Applied Energy*, vol. 90, no. 1, pp. 128–136, 2012.

[29] R. Pelc and R. M. Fujita, "Renewable energy from the ocean," *Marine Policy*, vol. 26, no. 6, pp. 471–479, 2002.

[30] P. Garcia-Rosa, J. Cunha, F. Lizarralde, S. Estefen, I. Machado, and E. Watanabe, "Wave-to-wire model and energy storage analysis of an ocean wave energy hyperbaric converter," *IEEE Journal of Oceanic Engineering*, vol. 39, no. 2, pp. 386–397, April 2014.

[31] E. Sanchez, R. Hansen, and M. Kramer, "Control performance assessment and design of optimal control to harvest ocean energy," *IEEE Journal of Oceanic Engineering*, vol. PP, no. 99, pp. 1–12, 2014.

[32] K. Rajagopalan and G. C. Nihous, "Estimates of global ocean thermal energy conversion (OTEC) resources using an ocean general circulation model," *Renewable Energy*, vol. 50, no. 0, pp. 532 – 540, 2013.

[33] H. Chen, N. Ait-Ahmed, E. Zaim, and M. Machmoum, "Marine tidal current systems: State of the art," in *Industrial Electronics (ISIE), 2012 IEEE International Symposium on.* IEEE, 2012, pp. 1431–1437.

[34] S. E. Skilhagen, J. E. Dugstad, and R. J. Aaberg, "Osmotic powerpower production based on the osmotic pressure difference between waters with varying salt gradients," *Desalination*, vol. 220, no. 1, pp. 476–482, 2008.

[35] Y. Li and H. Florig, "Modeling the operation and maintenance costs of a large scale tidal current turbine farm," in *OCEANS 2006*, Sept 2006, pp. 1–6.

[36] J. Liang and B. Whitby, "Field oriented control of a permanent magnet synchronous generator for use in a variable speed tidal stream turbine," in *Universities' Power Engineering Conference (UPEC), Proceedings of 2011 46th International*, Sept 2011, pp. 1–6.

[37] T. Delorm, D. Zappalà, and P. Tavner, "Tidal stream device reliability comparison models," *Proceedings of the Institution of Mechanical Engineers, Part O: Journal of Risk and Reliability*, vol. 226, no. 1, pp. 6–17, 2012.

[38] D. N. Walker, S. L. Adams, and R. J. Placek, "Torsional vibration and fatigue of turbine-generator shafts," *IEEE Trans. Power Apparatus and Systems*, vol. PAS-100, no. 11, pp. 4373–4380, Nov 1981.

[39] M. C. Jackson, S. Umans, R. Dunlop, S. H. Horowitz, and A. C. Parikh, "Turbine-generator shaft torques and fatigue: Part I - simulation methods and fatigue analysis," *IEEE Trans. Power Apparatus and Systems*, vol. PAS-98, no. 6, pp. 2299–2307, Nov 1979.

[40] T. Hammons, "Accumulative fatigue life expenditure of turbine/generator shafts following worst-case system disturbances," *IEEE Trans. Power Apparatus and Systems*, vol. PAS-101, no. 7, pp. 2364–2374, July 1982.

[41] J. Song-Manguelle, S. Schroder, T. Geyer, G. Ekemb, and J. Nyobe-Yome, "Prediction of mechanical shaft failures due to pulsating torques of variable-frequency drives," *IEEE Trans. Industry Applications*, vol. 46, no. 5, pp. 1979–1988, Sept 2010.

[42] C. Luo, H. Banakar, B. Shen, and B.-T. Ooi, "Strategies to smooth wind power fluctuations of wind turbine generator," *IEEE Trans. Energy Conversion*, vol. 22, no. 2, pp. 341–349, June 2007.

[43] Z. Zhao, P. Zhang, J.-H. Cui, and S. Zhou, "Life-oriented control of tidal power generation," in *Oceans - San Diego, 2013*, Sept 2013, pp. 1–5.

[44] M. Khan, G. Bhuyan, M. Iqbal, and J. Quaicoe, "Hydrokinetic energy conversion systems and assessment of horizontal and vertical axis turbines for river and tidal applications: A technology status review," *Applied Energy*, vol. 86, no. 10, pp. 1823–1835, 2009.

[45] A. Mason-Jones, D. M. O'Doherty, C. E. Morris, T. O'Doherty, C. Byrne, P. W. Prickett, R. I. Grosvenor, I. Owen, S. Tedds, and R. Poole, "Non-dimensional scaling of tidal stream turbines," *Energy*, vol. 44, no. 1, pp. 820–829, 2012.

[46] S. Benelghali, M. Benbouzid, and J. Charpentier, "Comparison of PMSG and DFIG for marine current turbine applications," in *Electrical Machines (ICEM), 2010 XIX International Conference on*, Sept 2010, pp. 1–6.

[47] O. Keysan, M. Mueller, A. McDonald, N. Hodgins, and J. Shek, "Designing the c-gen lightweight direct drive generator for wave and tidal energy," *IET Renewable Power Generation*, vol. 6, no. 3, pp. 161–170, 2012.

[48] O. Keysan, A. McDonald, and M. Mueller, "A direct drive permanent magnet generator design for a tidal current turbine(seagen)," in *Electric Machines Drives Conference (IEMDC), 2011 IEEE International*, May 2011, pp. 224–229.

[49] S. Benelghali, M. El Hachemi Benbouzid, J. Charpentier, T. Ahmed-Ali, and I. Munteanu, "Experimental validation of a marine current turbine simulator: Application to a permanent magnet synchronous generator-based system second-order sliding mode control," *IEEE Trans. Industrial Electronics*, vol. 58, no. 1, pp. 118–126, Jan 2011.

[50] H. Chen, N. Ait-Ahmed, M. Machmoum, M. Zaim, and E. Schaeffer, "Modeling and current control of a double salient permanent magnet generator (DSPMG)," in *Power Electronics and Applications (EPE), 2013 15th European Conference on.* IEEE, 2013, pp. 1–10.

[51] A. Carlsson. (1998, May) The back to back converter, control and design. [Online]. Available: http://www.iea.lth.se/publications/Theses/LTH-IEA-1017.pdf

[52] A. Mullane, G. Bryans, and M. O'Malley, "Kinetic energy and frequency response comparison for renewable generation systems," in *Future Power Systems, 2005 International Conference on*, Nov 2005, pp. 6 pp.–6.

[53] M. Jahromi, A. Maswood, and K.-J. Tseng, "Design and evaluation of a new converter control strategy for near-shore tidal turbines," *IEEE Trans. Industrial Electronics*, vol. 60, no. 12, pp. 5648–5659, Dec 2013.

[54] C. F. Lorenzo and W. Merrill, "Life extending control - a concept paper," in *American Control Conference, 1991*, June 1991, pp. 1081–1095.

[55] C. Stillinger, T. Brekken, and A. von Jouanne, "Furthering the study of real-time life extending control for ocean energy conversion," in *Power and Energy Society General Meeting, 2012 IEEE*, July 2012, pp. 1–9.

[56] C. Stillinger, T. Brekken, A. von Jouanne, R. Paasch, D. Naviaux, K. Rhinefrank, J. Prudell, A. Schacher, and E. Hammagren, "WEC prototype advancement with consideration of a real-time damage accumulation algorithm," in *PowerTech, 2011 IEEE Trondheim*, June 2011, pp. 1–8.

[57] Z. Zhou, F. Scuiller, J. Charpentier, M. Benbouzid, and T. Tang, "Power limitation control for a PMSG-based marine current turbine at high tidal speed and strong sea state," in *Electric Machines Drives Conference (IEMDC), 2013 IEEE International*, May 2013, pp. 75–80.

[58] Z. Zhou, F. Scuiller, J. F. Charpentier, M. Benbouzid, and T. Tang, "Grid-connected marine current generation system power smoothing control using supercapacitors," in *IECON 2012-38th Annual Conference on IEEE Industrial Electronics Society*. IEEE, 2012, pp. 4035–4040.

[59] Z. Zhou, F. Scuiller, J. Charpentier, M. El Hachemi Benbouzid, and T. Tang, "Power smoothing control in a grid-connected marine current turbine system for compensating swell effect," *IEEE Trans. Sustainable Energy*, vol. 4, no. 3, pp. 816–826, July 2013.

[60] M. H. Beale, M. T. Hagan, and H. B. Demuth. (2014, March) Neural network toolbox user's guide. [Online]. Available: http://www.mathworks.com/help/pdf_doc/nnet/nnet_ug.pdf

[61] K. Liu and Z. Zhu, "Online estimation of the rotor flux linkage and voltage-source inverter nonlinearity in permanent magnet synchronous machine drives," *IEEE Trans. Power Electronics*, vol. 29, no. 1, pp. 418–427, Jan 2014.

[62] S. Ariduru, "Fatigue life calculation by rainflow counting method," Master's thesis, Middle East Technical University, Ankara, Turkey, 2004.